

## Chapter 6

### Intrinsic and Aluminium Doped Zinc Oxide: Passivator and Charge collector

#### 6.0 Motivation, Objective, and Abstract

##### Motivation

The exact contribution of a unique, i. e., intrinsic Zinc Oxide (i-ZnO) layer in the performance of the CIGS solar cell module is still eccentric. Partly, i-ZnO has been figured out to be as an intermediary mitigator for lattice mismatch and bandgap discontinuity between the buffer and top window layer. Besides, it passivates the buffer layer. The transparent conductive layer has a distinct responsibility of charge collection and Aluminium Doped Zinc Oxide has proven itself as the best candidate. But on a large area (module) uniformity and resistivity are still quizzed.

##### Objective

- To prepare an in-house 2-inch (diameter) low-cost intrinsic-Zinc Oxide sputter target.
- To functionalize the intrinsic-Zinc Oxide sputter target for the optimization of the intrinsic layer between the buffer and top window layer.
- To assess the physical, microstructural, electrical, and optical properties of Aluminum doped Zinc Oxide appropriate for good charge collection.
- To measure the degree of disorder ‘Urbach Energy’ for both Intrinsic and Aluminium doped Zinc Oxide layer.

##### *Abstract*

*For fabrication of multilayer Copper Indium Gallium Diselenide (CIGS) thin-film solar cell module, intrinsic-Zinc Oxide and Aluminium doped Zinc oxide*

*thin film have been deposited using RF sputtering technique on 60 x 60 x 1mm SLG substrate. We have in house fabricated 2 inch-diameter i-ZnO sputter target for deposition of i-ZnO thin films. Optimization of i-ZnO thin films has been carried out using variable deposition parameters such as power, pressure, and thickness. Structural, optical, electrical, Urbach energy and Photoluminescence studies of highly resistive i-ZnO layer and transparent conductive oxide (AZO) layer thin films have been carried out. Resistivity  $6.8 \times 10^5 \Omega\text{-cm}$  and optical transmittance of about 92 % have been noted for i-ZnO thin films. For AZO thin film resistivity was  $6.26 \times 10^{-4} \Omega\text{-cm}$  and optical transmittance 85-90 %. Urbach energy was found in the range of 0.7 meV-3.0 meV and 0.766 meV-2.589 meV for all i-ZnO and AZO thin films. Photoluminescence spectra show an emission peak near UV for i-ZnO thin films and AZO thin films with less intense green luminescence. Raman spectra confirm the wurtzite structure with the presence of optical mode for i-ZnO and AZO thin films.*

## **6.1 High Resistive and Top conductive: i-ZnO and AZO**

An intrinsic-zinc oxide (i-ZnO) and Aluminium doped Zinc Oxide (AZO) layer has gained quite significant attention in the semiconductor industry. A wide range of its applications includes a light-emitting diode, sensors, thin-film transistors, photodetectors, laser diodes, etc. [1-5]. i-ZnO and AZO have wide and direct bandgap i. e. 3.2 eV and 3.35 eV near UV spectral range, high resistance, and transmission. Apart from these properties, i-ZnO and AZO have high electron mobility, thermal conductivity, and large exciton binding energy, which make them suitable for multi-variant semiconductor devices. One of their prominent applications is in the fabrication of thin-film solar cells. The i-ZnO layer is used as a highly resistive layer between the Cadmium Sulphide (CdS) buffer layer and the top window layer of Aluminium doped ZnO [6] in Copper Indium Gallium Diselenide (CIGS) based thin-film solar cells. The key role of the i-ZnO layer in CIGS solar cells is to provide high shunt resistance, which in turn helps to increase FF,  $V_{oc}$ , and ultimately the efficiency of the solar cell [7]. AZO is used as a transparent conductive oxide top window layer. It helps to

capture incoming photons and it is manifest that it allows absorbing all photons at Copper Indium Gallium Diselenide (CIGS) layers. Not only in CIGS solar cell but also for Si, CdTe, Perovskite, and dye-sensitized solar cell AZO act as a top window layer [8-11]. The resistive nature of the i-ZnO layer minimizes the baleful effect of short circuit pathways in the presence of pinholes, which increase performance capacity and uniformity during large scale area production. i-ZnO layer in conjunction with buffer and top window conductive layer should be chosen to improve band bending in the CIGS layer itself and eliminate defect densities at the interfaces. RF-magnetron sputtering, spray pyrolysis, molecular beam epitaxy (MBE), metal-organic chemical vapor deposition (MOCVD), sol-gel, and photo-assisted atomic layer [12-17] deposition techniques are typically used to prepare i-ZnO and AZO layer. This work or main aim is to optimize the i-ZnO and AZO layer for CIGS solar cell. The experiments are carried out using the RF sputtering technique with a rotating substrate for homogeneous deposition of the thin film. The results of structural, microstructural, optical, electrical, and defect characterizations are obtained will be used to develop CIGS solar cell module using monolithic interconnection made by the P3 laser scribing process.

## **6.2 Experimental Details**

ZnO thin films have been deposited using an i-ZnO target of 2 inches in diameter, fabricated in-house. Initially, i-ZnO powder (Sigma Aldrich, 99.9 %) was cold-pressed in a 2-inch die by applying 8 Ton pressure. Further, the target was sintered at 1125 °C with a ramp-rate of 60 °C per hour and hold up for 24 hours. Slight color change has been observed in the target, but the target was found to be brittle. The sintering process was repeated twice and finally, a stable i-ZnO target was formed. The relative density of the i-ZnO target was found to be 88.2 %. Using these targets, i-ZnO thin films were deposited on the soda-lime glass substrate using RF sputtering technique using a magnetron sputtering system with frequency 13.56 MHz (HÜTTINGER Elektronik, 600 W, Germany). The substrate has been rotated perpendicular to the sputter target during a deposition for structural homogeneity. To optimize deposition

conditions of i-ZnO thin films, deposition parameters viz. deposition pressure (10, 5, and 1 mTorr), deposition RF power (PRF) (50, 100, and 150 W), and thickness (50, 70, and 90 nm) were varied. Optical, electrical, structural and photoluminescence characterization of i-ZnO thin films have been carried out. Ceramic ZnO target doped with 2 % Al<sub>2</sub>O<sub>3</sub> For AZO thin films, deposition pressure (0.5, 5, 10, and 15 mTorr), thickness (300, 400, and 500 nm), substrate temperature (ST) i. e. room temperature (RT) and 215 °C (ST-215 °C) and PRF was kept constant 100 W.

## **6.3 Results and Discussion**

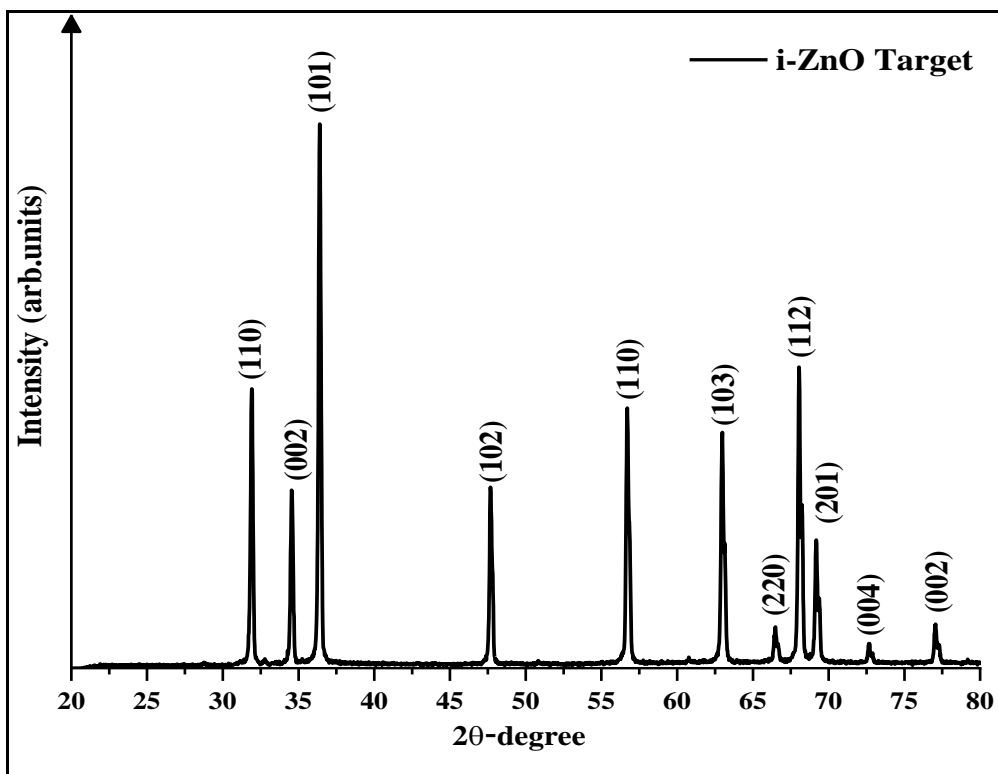
### **6.3.1 Structural Analysis**

X-ray diffraction analysis of the i-ZnO target shows the presence of all peaks of zinc oxide which are confirmed with JCPDS data card 36-1451. Before vacuum sintering thickness of i-ZnO was 7.35 mm while after sintering it reduces to 7.22 mm due to compactness of target and reduction in porosity. Photograph and XRD Pattern of 2-inch (diameter) i-ZnO Target is shown in Fig. 6.1. The structural analysis of i-ZnO thin films deposited using a 2-inch i-ZnO target is shown in Fig. 6.2. At deposition pressure (10, 5, and 1 mTorr) with different deposition power (50, 100, and 150 W) and thickness (50, 70, and 90 nm) X-ray diffraction analysis shows crystallographic changes in i-ZnO thin films. The films deposited at lower pressure i.e., 1 mTorr with different RF power and thickness, as shown in Fig. 6.2 (c), have improved crystallinity as compared to i-ZnO thin films deposited at higher deposition pressure, that is 10 mTorr and 5 mTorr as shown in Fig. 6.2 (a) and Fig. 6.2 (b). All i-ZnO thin films show a single major peak at  $2\theta$  value 34.68, which corresponds to the (002) phase [18]. The result has been confirmed with JCPDS-card no. (36-1451). There are slight deviations like intensity peak and width, which is mainly due to different growth conditions of i-ZnO thin films. We found no other additional peak in XRD analysis, which confirms the purity of the i-ZnO compound. Phase analysis of AZO thin films deposited at varied deposition parameters i. e. deposition pressure (0.5, 5, 10, and 15 mTorr), thickness (300, 400, and 500 nm) RF power

was kept constant at 100 W and RT and ST-215 °C has been plotted in Fig. 6.2 (d and e). X-ray diffraction spectrums of AZO thin films possess an ebb and flow pattern of the intensity of the major peak. (002) the phase was found for all AZO thin films at their major peak. No additional peak of Al, Zn, or Al<sub>2</sub>O<sub>3</sub> was detected, this confirms the pure phase formation of AZO. The only difference between all major peaks of AZO thin films was intensity, sharpness, FWHM value, and imperceptible change in 2θ values of the major peak. A pillar of the AZO phase is the base of the ZnO hexagonal structure. In the RT environment, low pressure 0.5 mTorr AZO thin films with different thicknesses of 300, 400, and 500 nm possess major peaks with low intensity and broad FWHM. On increasing pressure to 5 mTorr, AZO film with thickness 300 nm does not show a strong crystallographic phase along with preferred orientation; sudden improvement in the intensity of phase (002) was observed for 400 nm thickness as shown in Fig. 6.2 (d). The intensity of phase (002) remained constant for 500 nm thickness film also. On the subsequent increase in pressure 10 mTorr, only AZO thin film with a thickness of 400 nm possesses very sharp, the intense major peak having (002) phase at 2θ value 34.99 ° with FWHM 0.344 ° while for 300 nm and 500 nm thickness, the intensity of phase (002) decreases and FWHM broadening takes place [19]. A decrease in crystallinity was observed for AZO thin films deposited at 15 mTorr for 300, 400, and 500 nm thickness where FWHM broadening increase approximately to 0.724 °. The crystallinity of AZO thin films is affected not only by the substitution of donor Al<sup>3+</sup> instead of Zn<sup>2+</sup> cation but also due to deposition pressure and thickness. One another reason for poor crystallinity is stress development during the deposition process. The c-axis growth is preferred for AZO thin film to act as a window layer for CIGS solar cells. Not only RT, but AZO thin films deposited at ST-215 °C in Fig. 6.2 (e) shows a similar pattern of the major peak with phase (002) intensity at 2θ value 35.12 ° with FWHM 0.404 °. In presences of ST-215 °C shown in Fig. 2 (e) and 0.5 mTorr pressure AZO compound fails to grow along the c-axis with phase (002) for 300, 400, and 500 nm thickness. Even at other deposition pressure i. e., 10 and 15 mTorr there is no strong major peak found for either thickness except at 5 mTorr with 500 nm thickness.

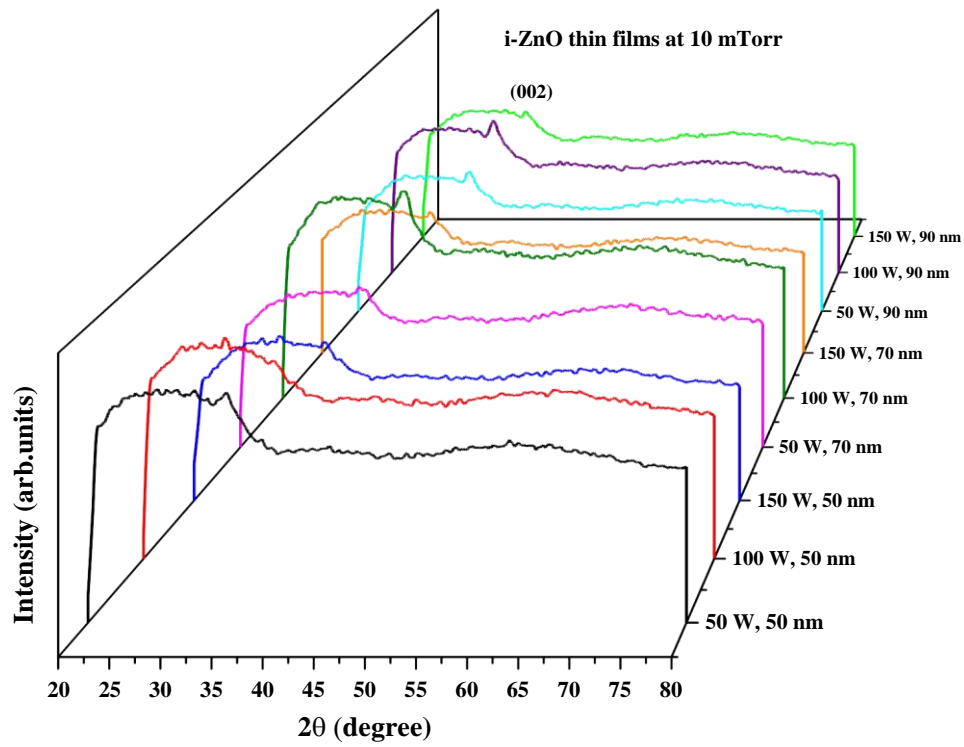


(a)

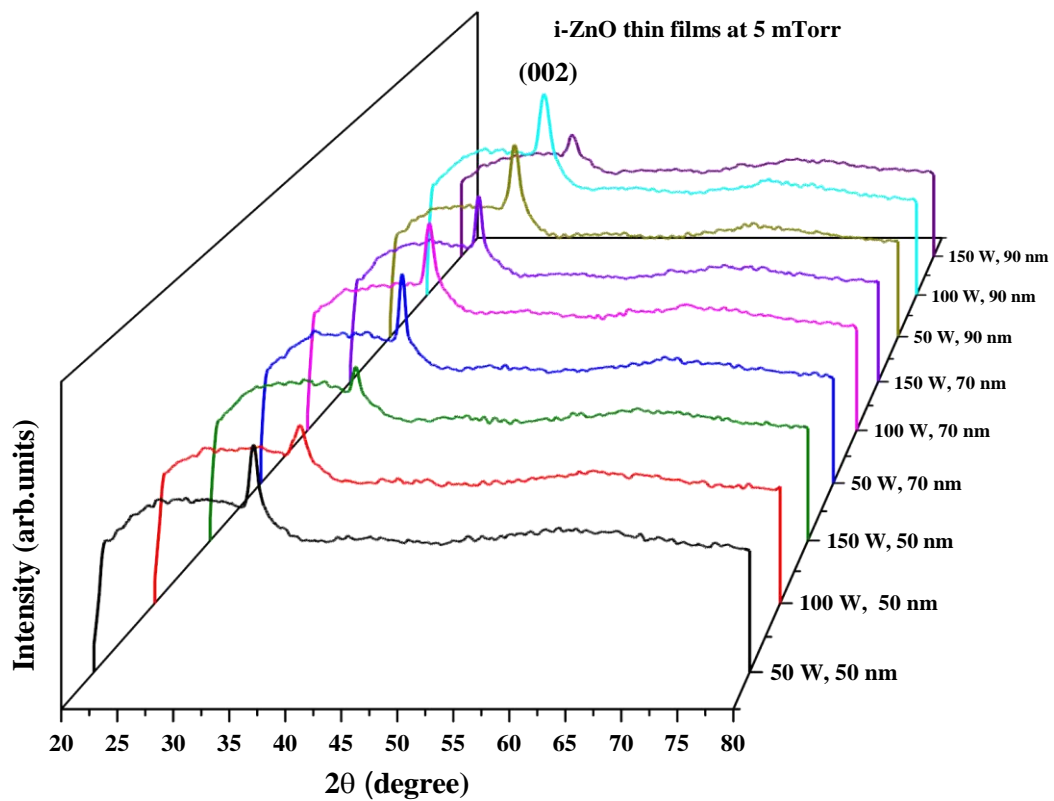


(b)

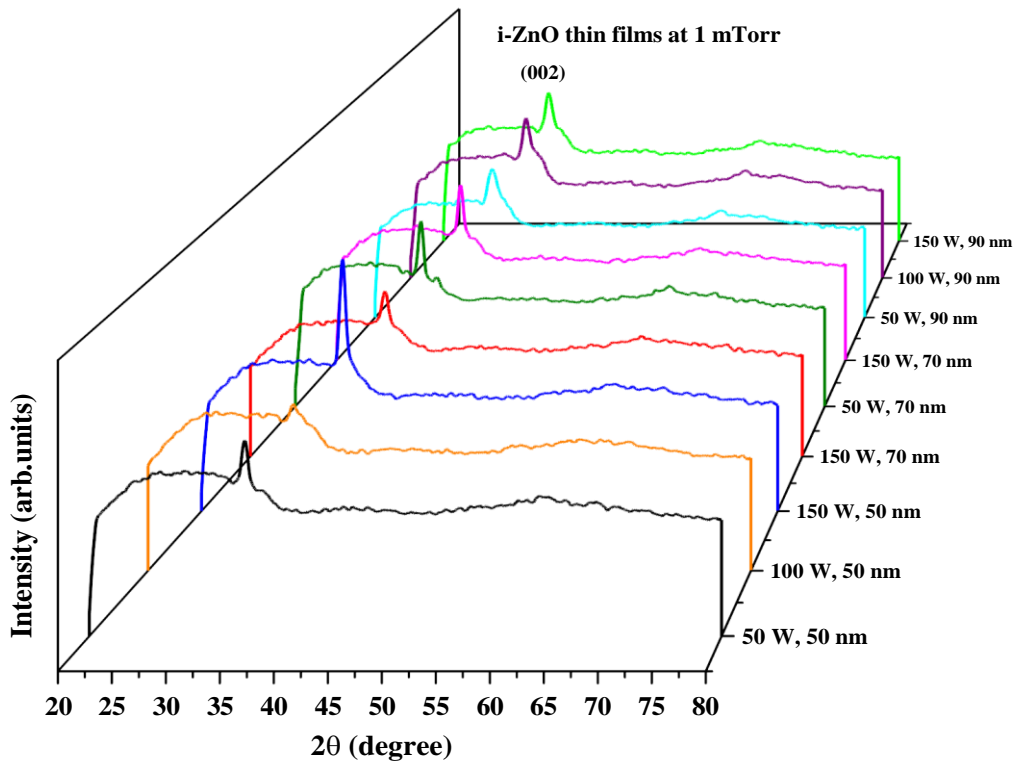
**Fig. 6.1: (a) Photograph and (b) XRD Pattern of 2-inch (diameter) i-ZnO Target.**



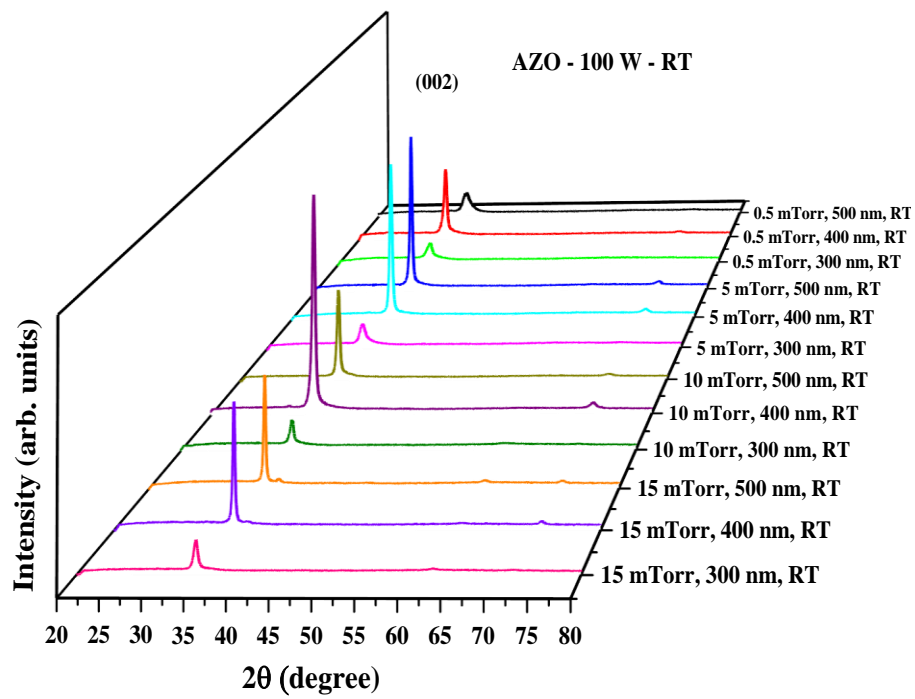
(a)



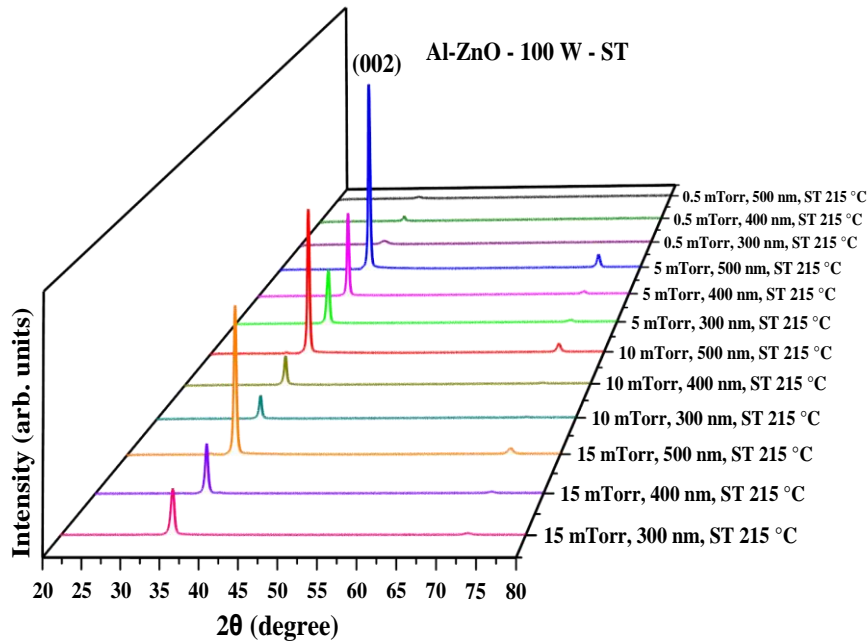
(b)



(c)



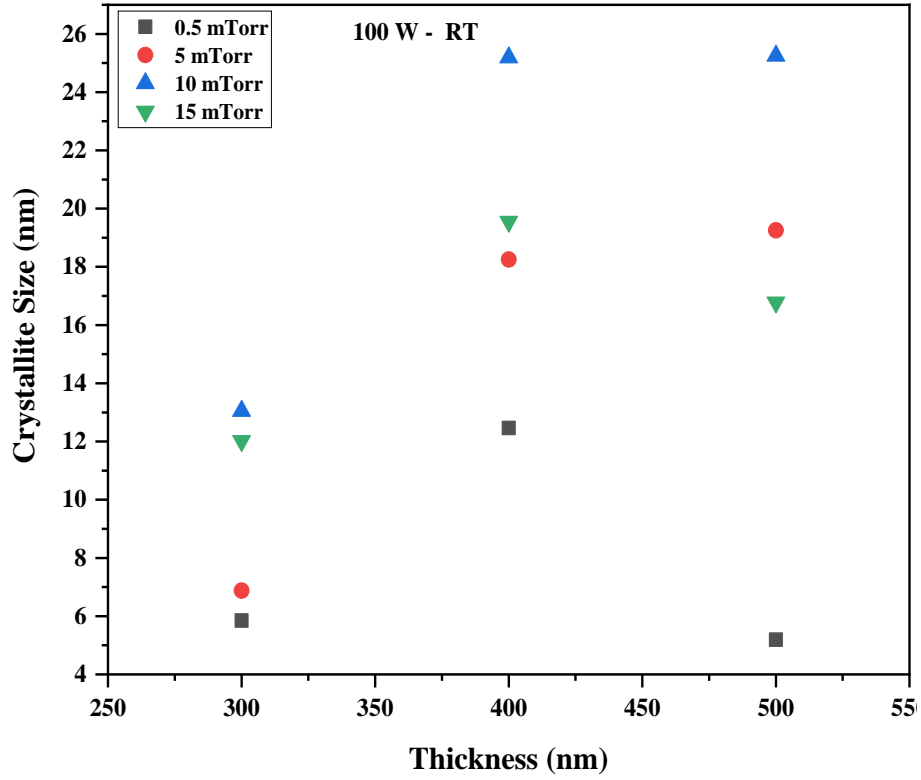
(d)



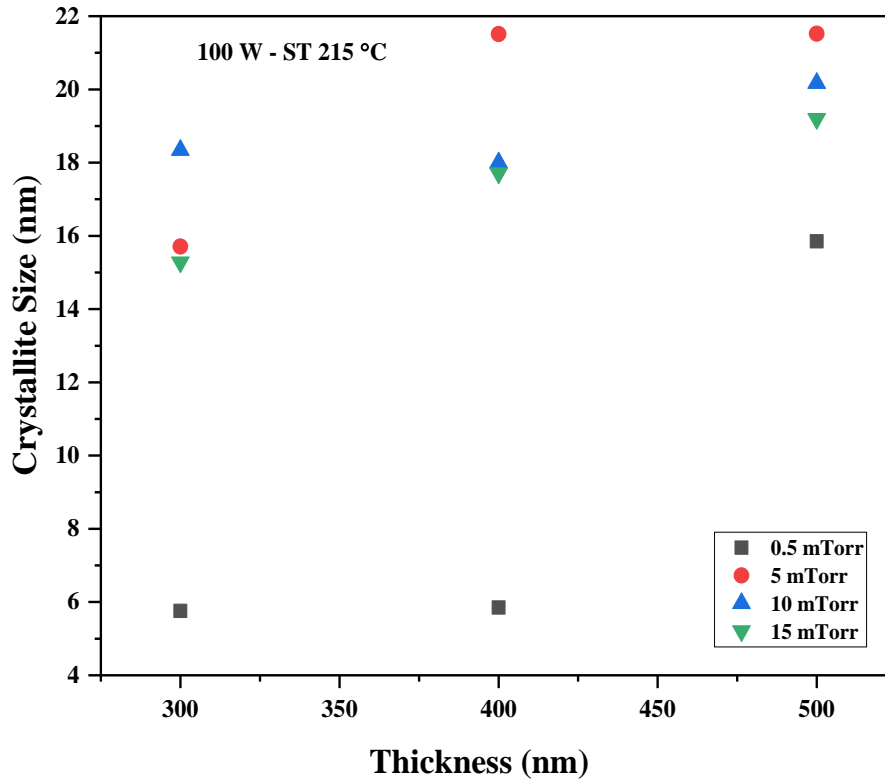
(e)

**Fig. 6.2: XRD analysis of RF sputtered i-ZnO (a, b, and c) and AZO (d and e) thin films deposited at variable deposition pressure and power, thickness, and substrate temperature.**

Using Scherrer's formula for crystallite size for i-ZnO and AZO thin films were estimated. Depending on deposition pressure, thickness, and ST crystallite size vary. Fig. 6.3 (a) and (b) represent the crystallite size of AZO thin films deposited at various deposition parameters. AZO thin films at 10 mTorr, 400 nm thickness have a crystallite size of about 25.18 nm, while at ST-215 °C, 5 mTorr and thickness 500 nm have 21.52 nm. As crystallinity improves, FWHM narrows down at  $2\theta$  value which results in enhancement of the crystallinity of thin-film. Additional factor such as substrate temperature promotes growth. Substrate temperature improves growth kinetics due to an increase in deposition rate. Once supersaturation of crystallite size takes place then on increasing lateral thickness of the thin film, no change in crystallite size was found for both AZO thin films deposited at RT and ST-215 °C.



(a)



(b)

**Fig. 6.3: Crystallite size of RF sputtered AZO thin films (a) RT and (b) ST-215 °C thin films deposited at variable deposition pressure and thickness.**

### 6.3.2 Optical Analysis

The optical analysis shows the transmittance characteristic of i-ZnO thin films. Transmittance has been carried out in near-UV to the visible range. The highest recorded transmittance is 94 % average in the visible region for i-ZnO thin films deposited at 1 mTorr, 100 W, and thickness 50 nm. High transmission for the i-ZnO layer is suitable for collecting more photons in CIGS solar cells. As the thickness increases, the transmission decreases for i-ZnO. The minimum energy required for an electron to excite from valence band to conduction band is known as optical bandgap. A sharp absorption edge is found at 374 nm, which corresponds to the optical bandgap of i-ZnO. There is a shift in the excitonic absorption edge at the higher thickness, which results due to defect formation in the crystallographic structure of i-ZnO. The optical bandgap of i-ZnO thin films was estimated by plotting Tauc's relation [20, 21]. Results of Tauc's plot for i-ZnO thin film varied from 3.0 to 3.63 eV. The bandgap energy for the highly crystallographic oriented i-ZnO thin film deposited at 1 mTorr, 100 W, and thickness 50 nm is found to be 3.36 eV. Fig. 6.4 (a), (b), and (c) show transmittance spectra of i-ZnO thin films deposited at pressure (10, 5, and 1 mTorr) with different deposition power (50, 100, and 150 W) and thickness (50, 70 and 90 nm). Average transmittance for all AZO thin films was about 85-90 % in the visible region was found. The sharp band edge was at 363 nm and it varies slightly for various deposition conditions. One can notice from Fig. 6.5 that the sharp band edge for AZO thin films is a function of deposition pressure and thickness. In Fig. 6.5 (a), AZO film with 300 nm thickness has a peak around 376 nm and transmittance remains constant over the entire visible region. On increasing thickness to 400 and 500 nm, multiple interference patterns were observed. No sharp band edge was found for AZO film with a thickness of 500 nm at 15 mTorr and ST-215 °C; peak wavelength was also distorted which confirms the poor crystallinity. As deposition pressure decrease to 10 mTorr shown in Fig. 6.5 (e and g), all AZO thin films sharp band edge and have a sharp peak around 384 nm. Of course, there was a shift in peak but there were multiple interference patterns due to homogeneity of the film except

for 300 nm thickness. Similar results were obtained for AZO films deposited at 5 and 0.5 mTorr. Redshift in peak wavelength was found for AZO thin films deposited at 0.5 mTorr and even their edge band was slightly stretch out forming a tail. Less interference pattern was observed for AZO thin film deposited at 5 and 0.5 mTorr, these results agree with XRD analysis results. Due to the doping of Al atoms in undoped ZnO, the bandgap of AZO film shifts towards lower as well as to higher wavelength. Bandgap for all AZO was estimated as shown in Fig. 6.5 (b, d, f, and h) and it was in the range of 2.88 to 3.25 eV. For AZO thin film deposited at 10 mTorr with 400 nm thickness at RT, the bandgap is 3.35 eV. This is true for the pure or intrinsic semiconductor material, but in the case of n-type doped wide bandgap semiconductor material bottom of conduction is filled by donor electrons. According to Fermi Exclusion Principle, a photon with higher energies allowed to make the vertical transition from the valence band to the conduction band, therefore blocking of low energy transition results in bandgap widening due to alteration in crystals because of charge carrier motion and their scattering against ionized impurity. This shift in bandgap is known as Burstein-Moss shift (BM shift) [22-27]. In n-type doped semiconductor optical bandgap is the summation of undoped semiconductor and BM shift is given by the following equation (6.1):

$$E_{\text{doped}} = E_{\text{undoped}} + E_{\text{BM}} \quad (6.1)$$

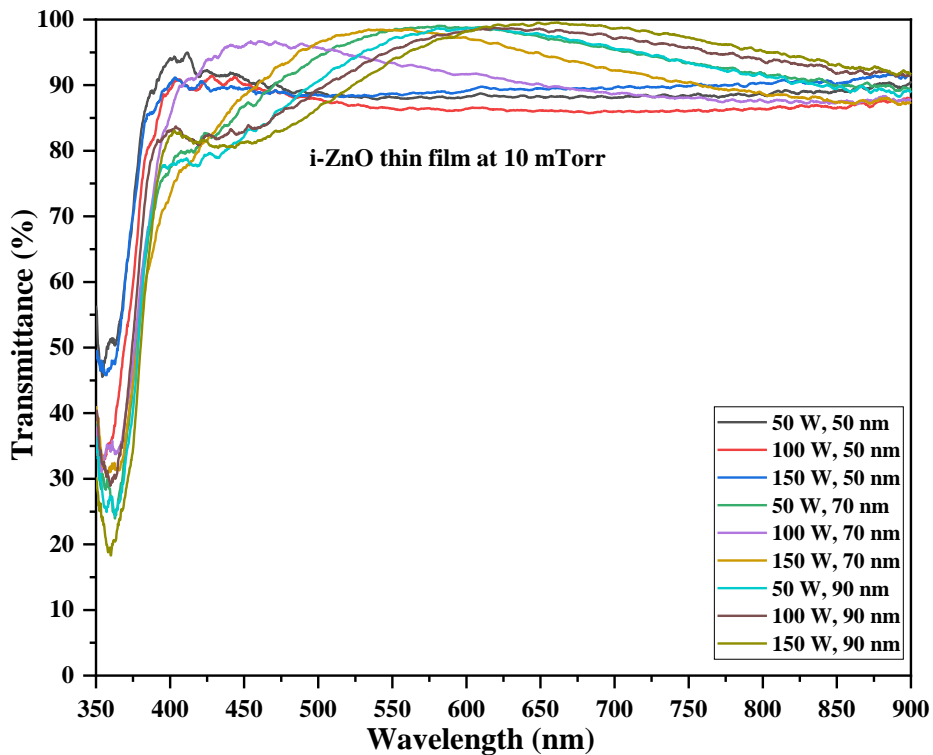
Conduction band minima are filled up by electrons on the addition of donor atoms. When conduction band density of states  $N_c$  is overpopulated than carrier concentration, it is expressed according to equation (6.2):

$$N_c = \frac{2(2m^*kT)^{3/2}}{h^3} \quad (6.2)$$

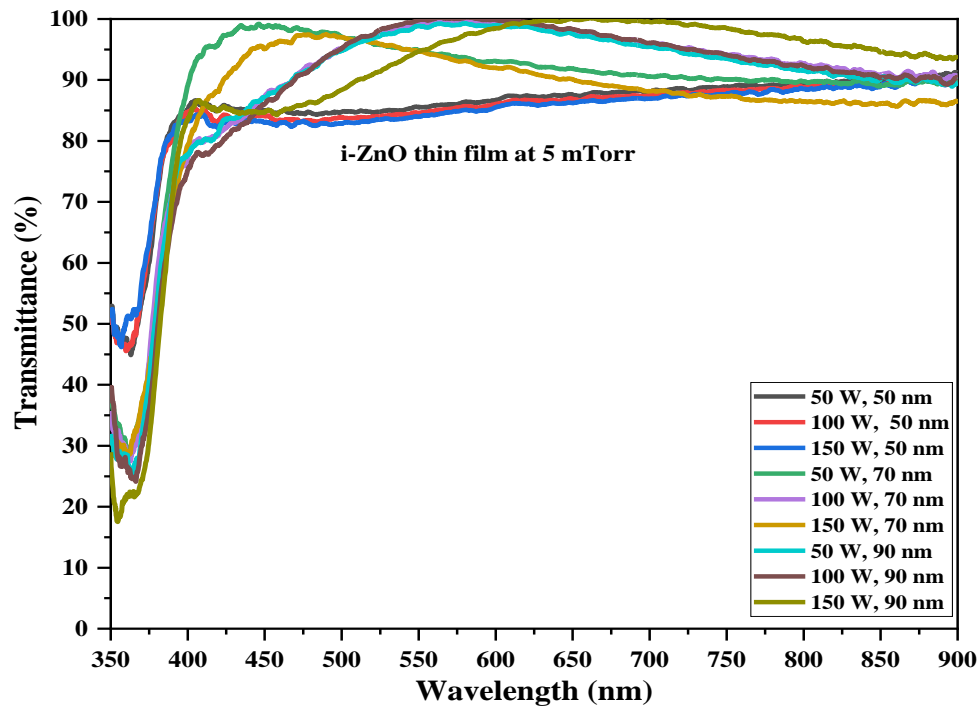
Where  $h$  is Planck's constant and  $m^*$  is the conduction band effective mass of the electron. Electron excitation from valence band electrons to above conduction band minima possesses interband transition. This creates a tail shift below the absorption edge and pushes the Fermi level to a higher energy level of a degenerate semiconductor. The shift in the tail is proportional to carrier concentration given by equation (6.3):

$$\Delta E_{BM} = \left[ \frac{h^2}{8m^*} \right] \left[ \frac{3n}{\pi} \right]^{2/3} \quad (6.3)$$

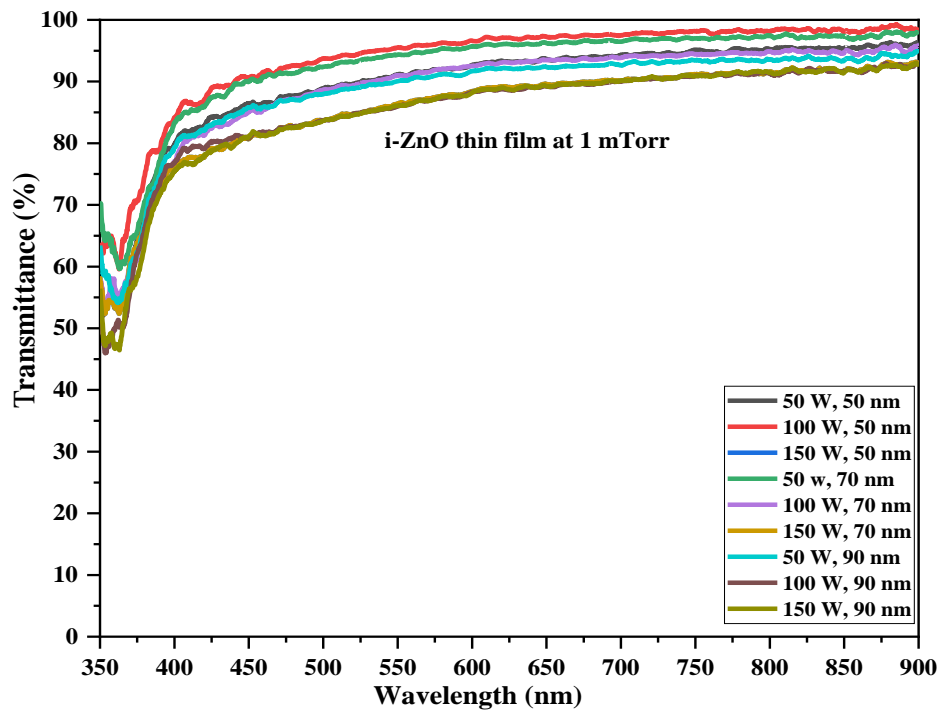
where  $m^* = 0.38 m_0$  for ZnO and hence carrier concentration (n) can be estimated for respective band shift. Form  $m^* = 0.38 m_0$ , the effective density of states  $N_c$  is approximately  $5.9 \times 10^{18} \text{ cm}^{-3}$  therefore carrier concentration (n) larger than  $N_c$  will possess optical band shift. The Bandgap widening of AZO thin film deposited at RT and ST-215 °C is shown in Fig. 6.6 (a and b). This kind of bandgap widening occurs because host atoms are charged due to displacement of charge from one to another atomic species. The charge in the crystal possesses displacement polarization due to the displacement of charge in it. The hole in the valence band is surrounded by a cloud of negative charge while the electron in the conduction band is surrounded by a positive charge. Each system of charge is viewed as a new particle, termed as polaron. Interaction in such polaron is ‘many-body interaction’ which results in self – energy shift due to displacement polarization. Not only band gap widening but narrowing of bandgap also takes place due to bandgap renormalization.



(a)

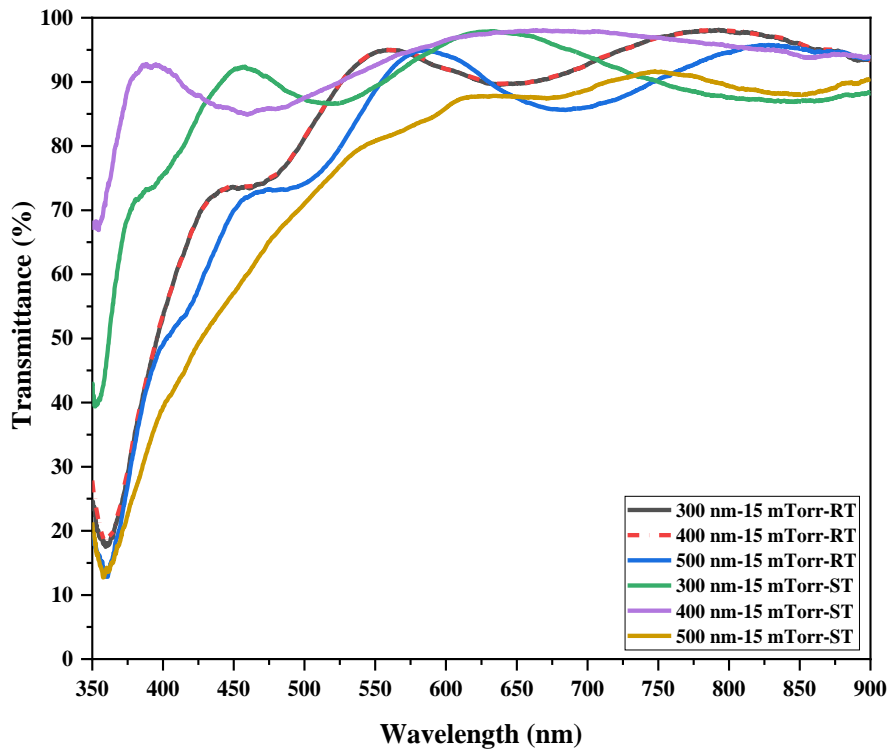


(b)

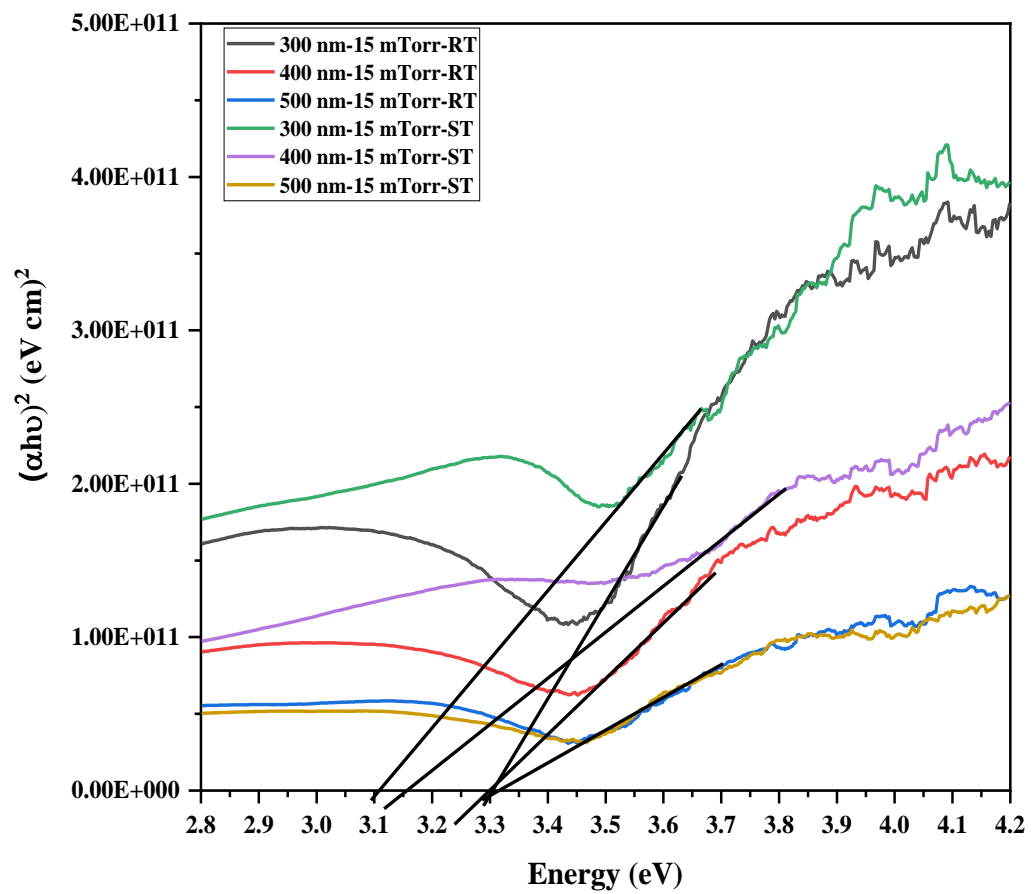


(c)

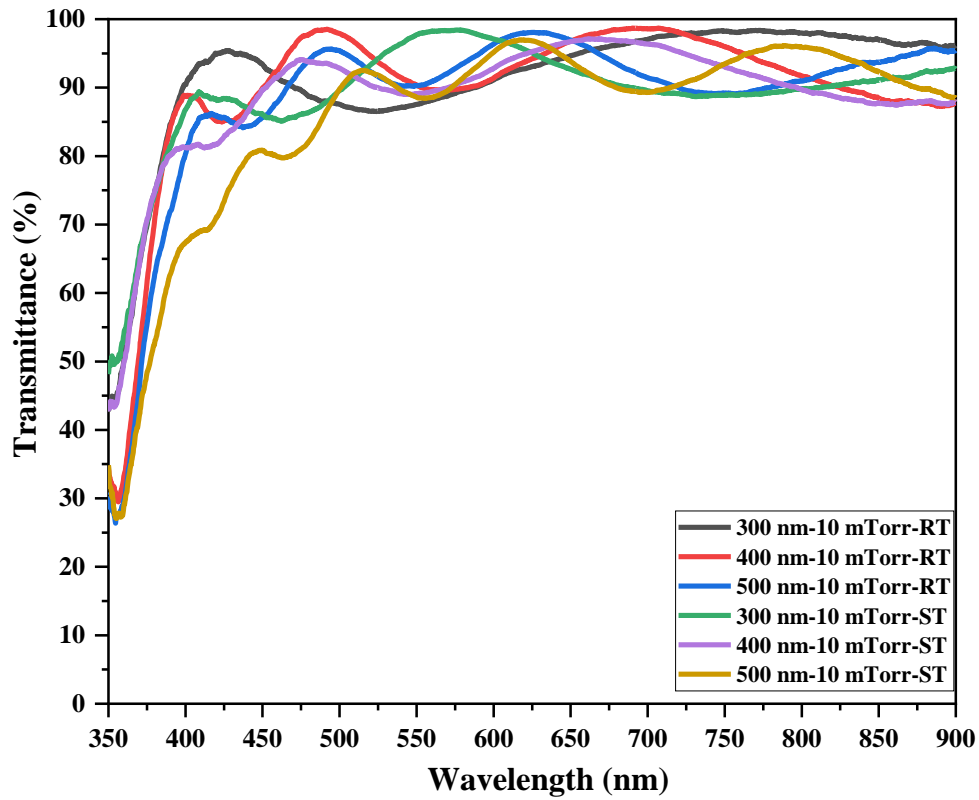
Fig. 6.4: Optical transmission spectra of i-ZnO thin films deposited ((a) 10, (b) 5 and (c) 1 mTorr), deposition power (50, 100 and 150 W) having thickness (50, 70 and 90 nm).



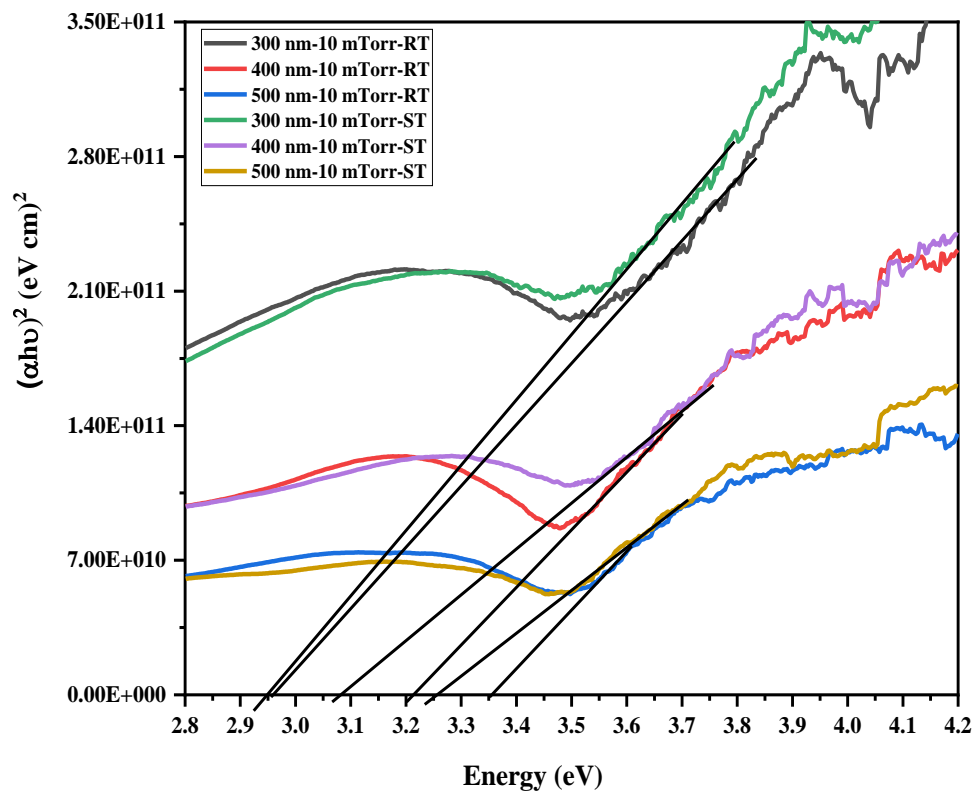
(a)



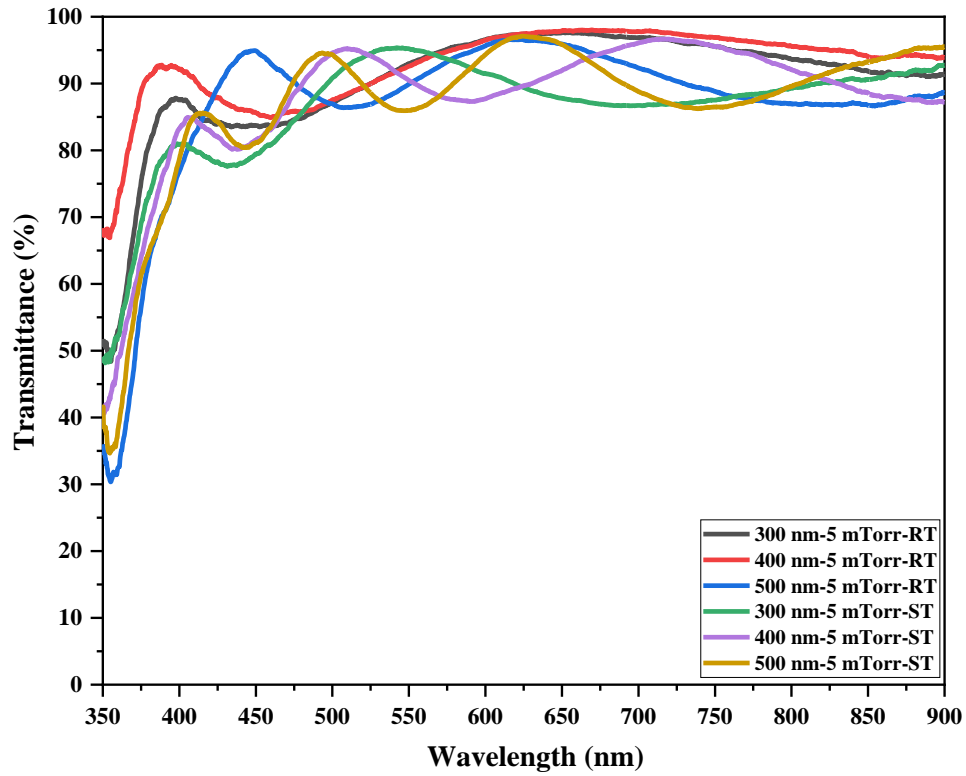
(b)



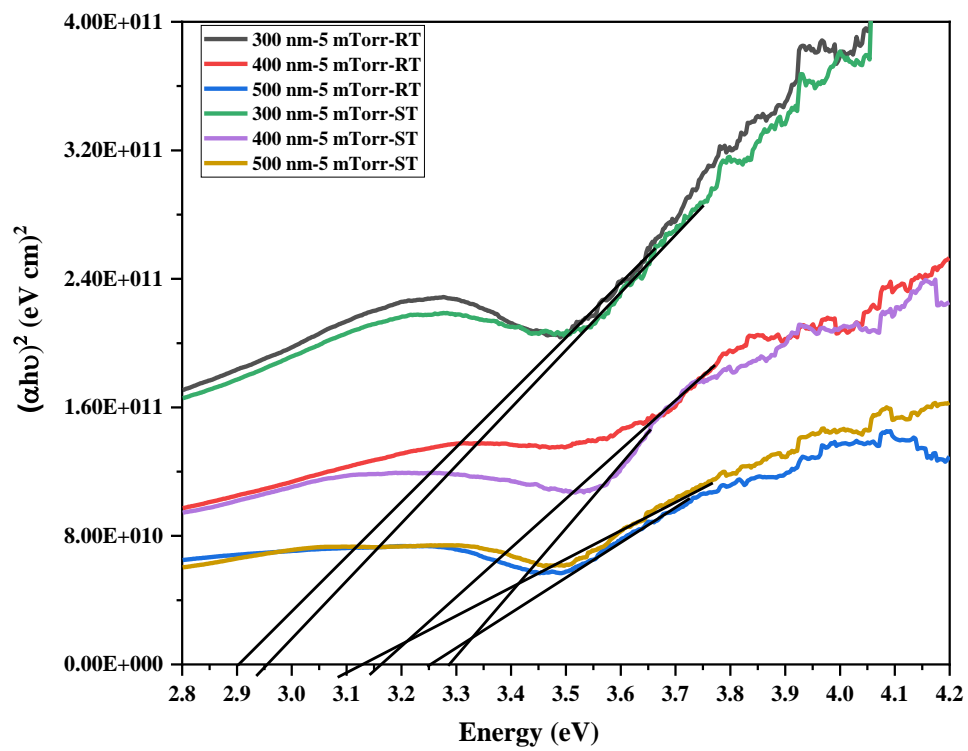
(c)



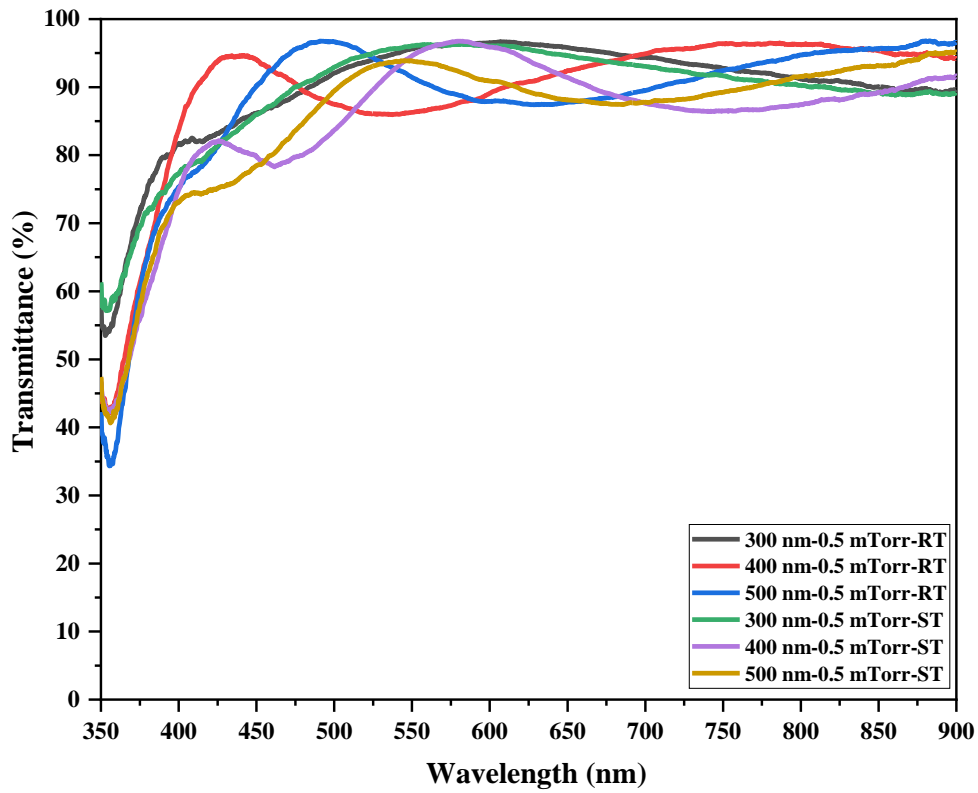
(d)



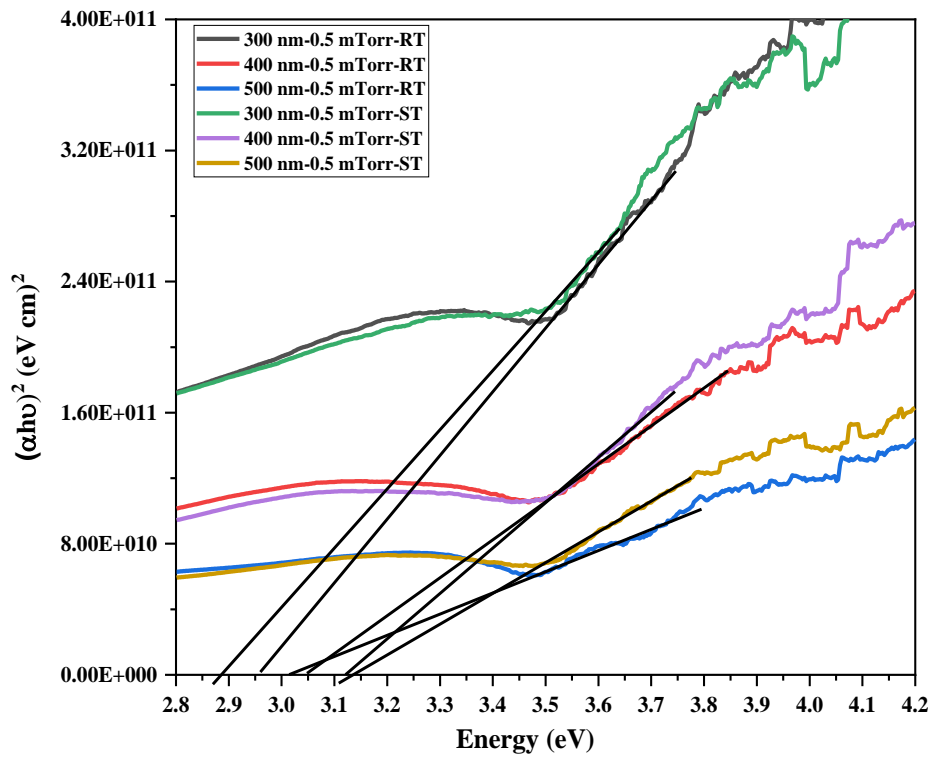
(e)



(f)

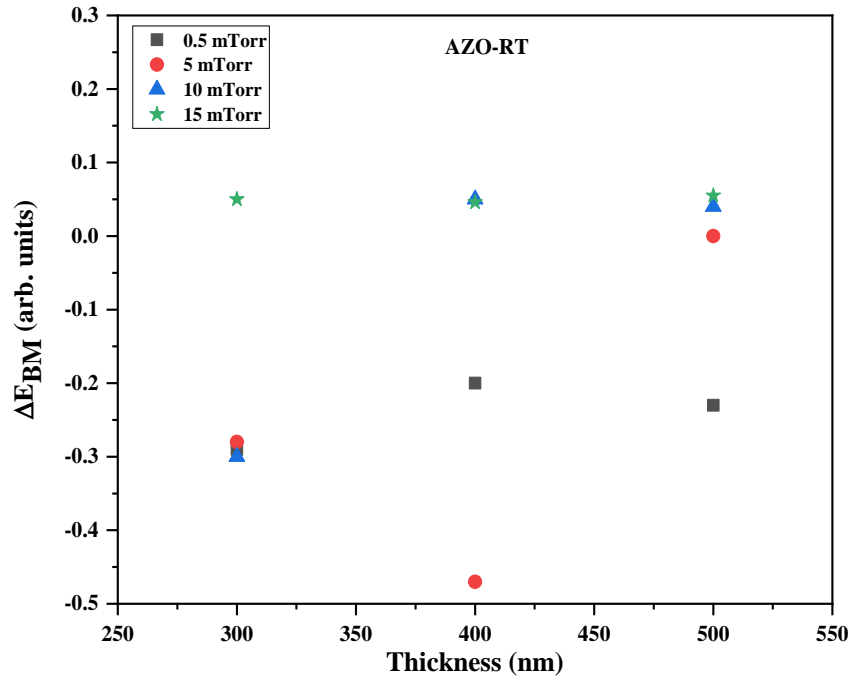


(g)

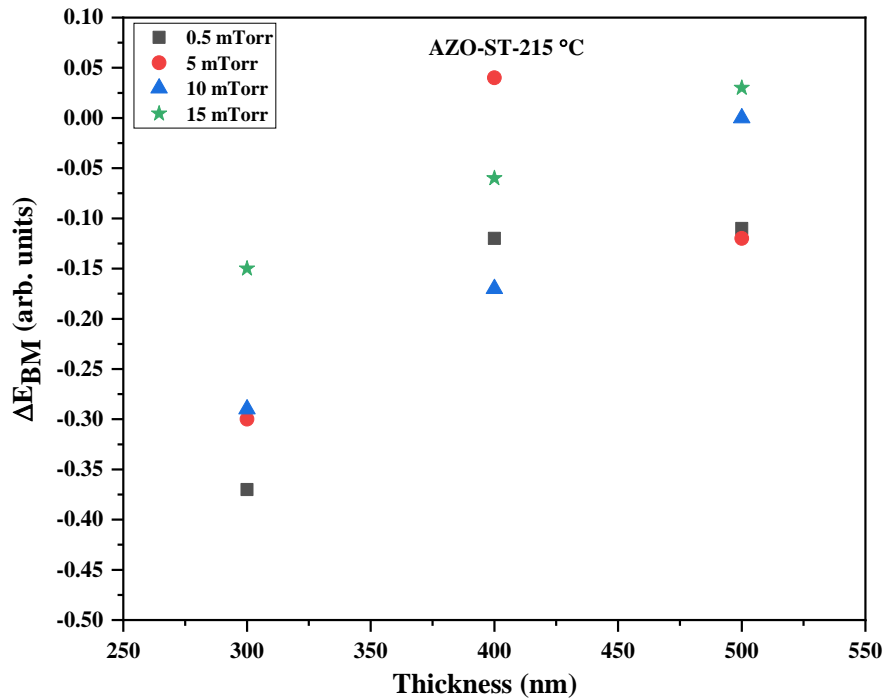


(h)

**Fig. 6.5: Optical transmittance and Bandgap spectra of AZO thin films deposited (15 (a and b),10 (c and d), 5 (e and f) and 1 (g and h) mTorr), deposition power 100 W having a thickness (300, 400 and 500 nm).**



(a)



(b)

**Fig. 6.6: Burstein-Moss shift of AZO thin films (a) RT and (b) ST-215 °C.**

### **6.3.3 Urbach Energy and Electrical Measurements**

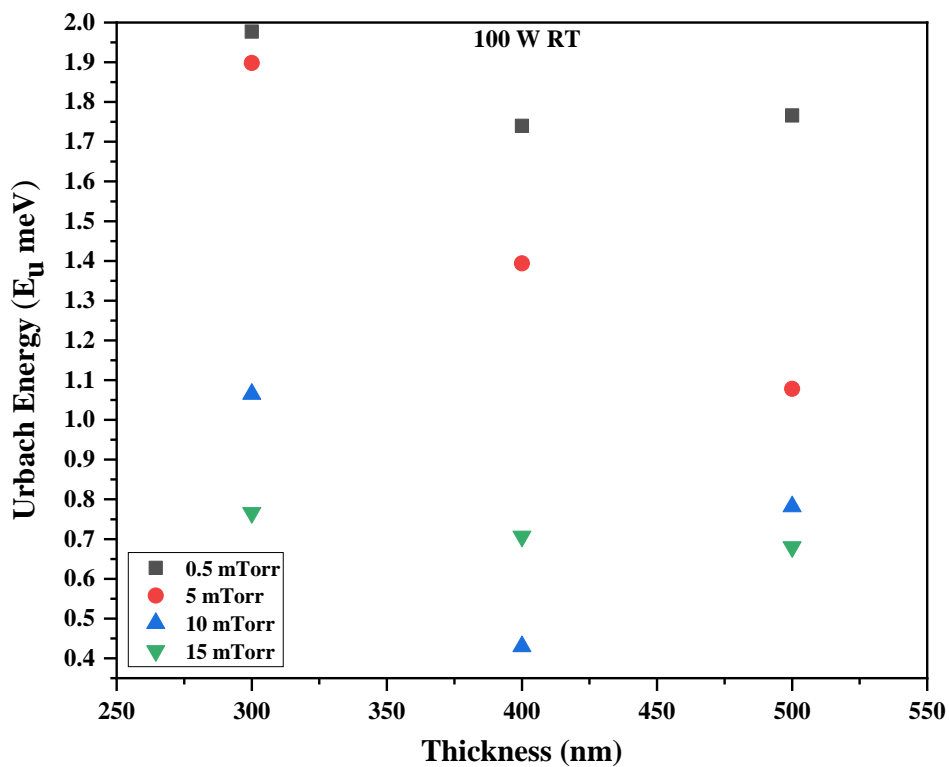
Urbach energy is the measure of disorder in material. Below the excitonic absorption edge, the Urbach tail is observed. The causes of defect disorders associated with Urbach energy investigated over the years are structural disorders during growth procedure, external temperature, phonons, impurities, excitons, etc. [28, 29]. The deviation from ideal stoichiometry attributes to structural disorder. Urbach tail or width (meV) falls exponentially below the absorption edge or bandgap, known as the ‘Sub-band gap’. At incident photon energy  $h\nu$ , the absorption coefficient ‘ $\alpha$ ’ was measured. To estimate Urbach width,  $\ln(\alpha)$  versus energy should be plot followed by the linear fitting. Urbach's energy relation concerning the absorption coefficient is given in equation 6.4. The inverse of a slope will give Urbach width ( $E_u$ ). As the Urbach energy is associated with defect energy, low Urbach energy is preferable for good stoichiometry. Urbach energy or tail width for all i-ZnO thin film has been estimated in Table 6.1. The lowest Urbach energy estimated is for the i-ZnO thin film deposited at 1 mTorr, 151 W, and thickness 50 nm, which is 0.702 meV. This infers that at this deposition condition, the i-ZnO thin film has fewer defects in it compared to i-ZnO thin films deposited at other conditions. This result agrees with the structural and optical analysis. At low deposition pressure and high power, the incoming species of zinc and oxygen atoms occupy their favourable site at the surface of the substrate. They are thermodynamically stable for suitable growth at the (002) axis forming a hexagonal structure. This leads to less formation of intrinsic defects or vacancies in the final structure. Urbach energy in AZO thin film was estimated similarly to i-ZnO thin films. Fig. 6.7 (a and b) represent Urbach energy for AZO thin film deposited at variable pressure and thickness with PRF 100 W at RT and ST-215 °C. Urbach energy estimated for AZO thin film deposited at 10 mTorr, 100 W at RT with thickness 400 nm is 0.4302 meV and results are well in agreement with XRD report of same AZO film having a highly crystallographic orientation in (002) plane [30]. In the case of AZO thin film deposited at ST-215 °C, Urbach energy increased to 0.7298 meV compare to AZO deposited at RT but still, it is low

compare to all AZO film deposited at ST-215 °C, J. I. Pankove [31] reported that generation of Urbach tail and energy associated with may due to following reason: (1) At high impurity concentrations formation of impurity takes place, (2) presence of impurities and dislocation or disorder creates crystal imperfections and (3) combination of electron impurity and non-homogenous distribution of impurities. The equation (3.4) for Urbach energy is given below:

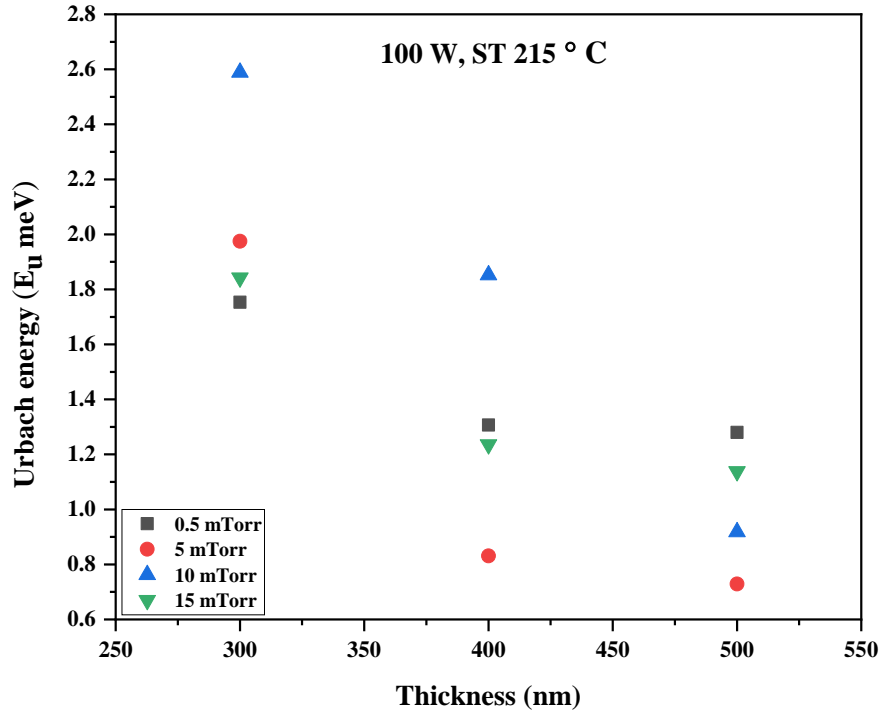
$$\alpha = \alpha_0 \left[ \frac{\left( \frac{E_g}{kT} \right)}{\beta} \right] \quad (6.4)$$

**Table 6.1: Urbach energy or ‘tail width’ of i-ZnO thin films at different deposition conditions.**

Thickness (nm)	Power (W)	10 (mTorr)	5 (mTorr)	1 (mTorr)
		E <sub>u</sub> (meV)		
50	50	0.762	1.891	1.452
	100	2.096	2.753	0.882
	150	1.398	2.886	0.702
70	50	0.909	1.279	1.140
	100	1.275	1.138	1.550
	150	0.906	1.379	1.084
90	50	1.055	0.941	1.011
	100	0.871	1.138	0.940
	150	0.980	0.863	2.993



(a)



(b)

**Fig. 6.7: Urbach Energy ( $E_U$ ) of RF sputtered AZO thin films (a) RT and (b) ST-215 °C thin films deposited at variable deposition pressure and thickness.**

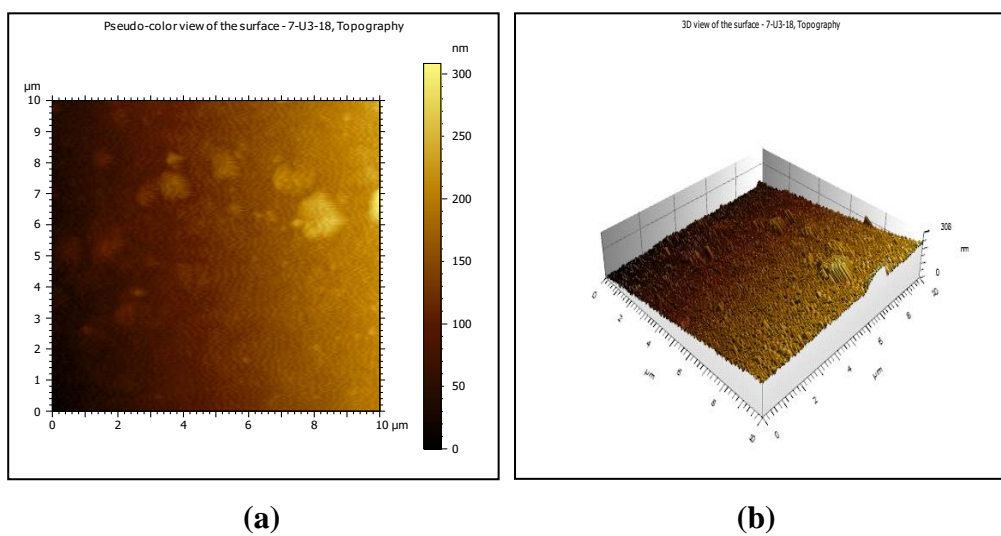
ZnO crystals have n-type of conductivity which is still a topic of debate. Controlling unintentional conductivity in ZnO crystal is a very challenging issue. The small concentration of different native point defects, such as antisite, vacancies, and the interstitial defect may give rise to unintentional conductivity which can significantly affect the electrical properties. Researchers have found that oxygen is a deep donor, which is responsible for the oxygen vacancy defect [32]. Another contribution for conductivity is the Hydrogen element, which acts as a shallow donor generating interstitial vacancy. The four-point probe method is used to characterize the electrical property of i-ZnO and AZO thin films. The highest resistivity measured was  $6.8 \times 10^5 \Omega\text{-cm}$  for an i-ZnO thin film with a thickness of 50 nm having depositing pressure of 1 mTorr and power 150 W. At low pressure and high PRF, the Zn and O atoms unite to form a ZnO hexagonal structure with controlled oxygen constituents leads to high resistivity. Whereas at high pressure and low PRF, there are formation defects and vacancy which decrease resistivity. Table 6.2 represents the electrical

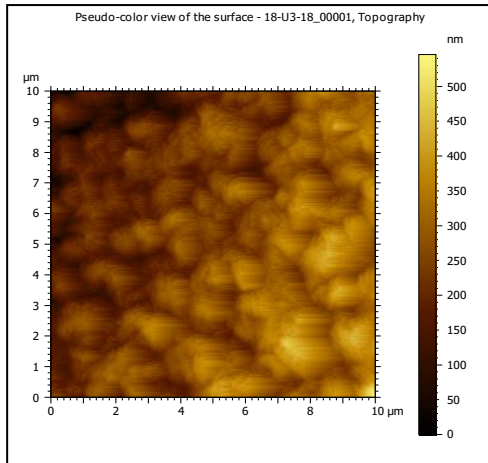
resistivity, Hall mobility, and carrier concentration of AZO thin films deposited at varied parameters. It was observed with an increase in deposition pressure up to 10 mTorr mobility and carrier concentration increase and then it decreases for 15 mTorr. Substrate temperature 215 °C improves the crystallinity as well as reduces the grain boundary. This results in low resistivity, high mobility, and carrier concentration. The results are acceptable compared to [33-35] having a magnitude of order  $10^{-4}$ .

**Table 6.2: Electrical resistivity, Hall Mobility, and Carrier concentration of AZO thin films deposited at  $P_{RF}$  100W.**

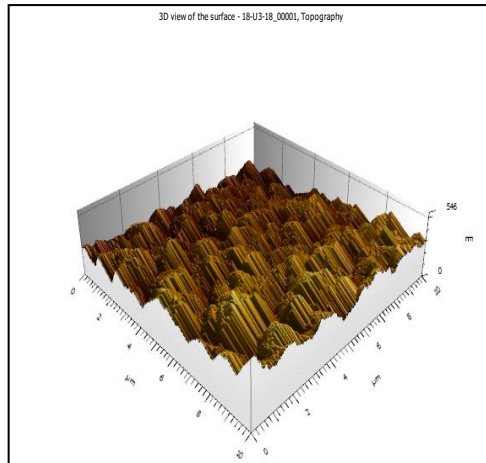
Parameters	Thickness (nm)	0.5 (mTorr)			5 (mTorr)			10 (mTorr)			15 (mTorr)		
		$\rho$ $\times 10^{-3}$ $\Omega\text{-cm}$	$\mu$ $(\text{cm}^2/\text{V-s})$	$n$ $\times 10^{19}$ $(\text{cm}^{-3})$									
RT	300	5.463	27.01	4.23	3.479	24.39	7.36	4.946	35.06	3.60	13.00	29.64	1.620
	400	7.175	34.61	2.50	2.609	37.41	6.41	0.626	42.06	23.7	17.30	38.23	0.952
	500	6.432	22.01	441	3.805	23.69	694	1.087	25.30	22.7	11.80	26.02	2.030
ST-215 °C	300	3.420	28.71	6.36	0.413	28.39	53.2	0.198	36.77	85.6	0.274	37.82	60.20
	400	0.920	40.91	16.5	0.250	47.50	52.5	0.250	49.08	50.9	0.300	49.66	41.80
	500	14.00	29.43	1.51	0.212	51.85	56.6	0.280	50.73	43.9	0.231	45.39	59.60

### 6.3.4 Atomic Force Microscopy Analysis

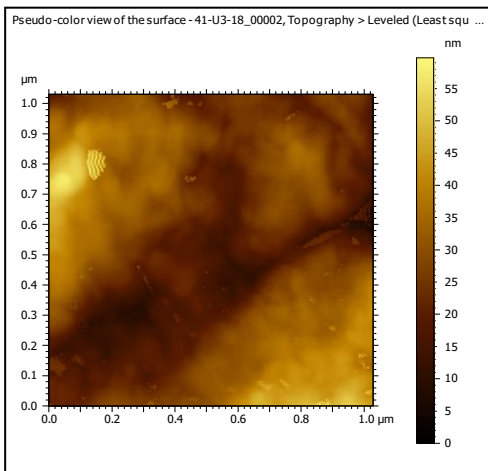




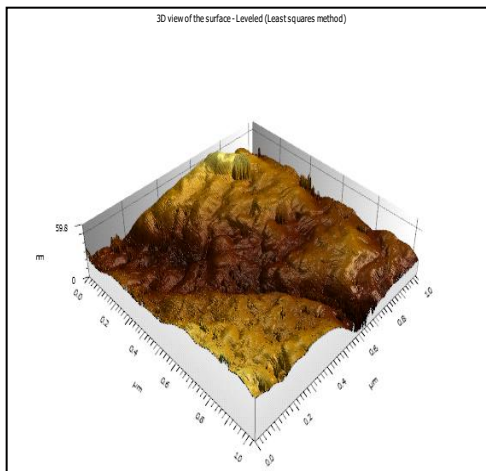
(c)



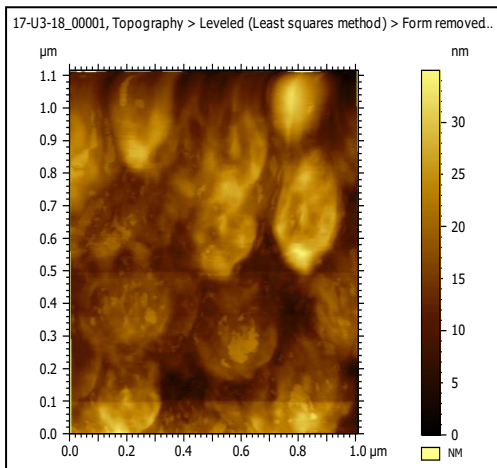
(d)



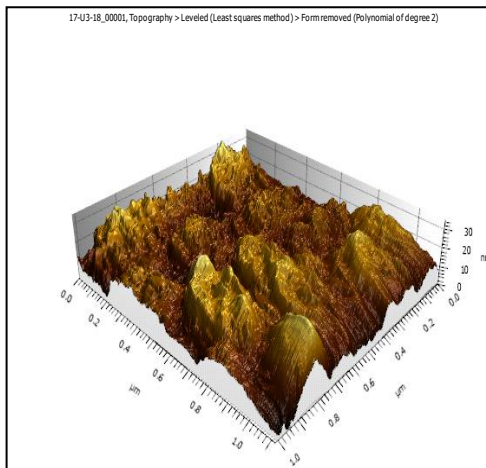
(e)



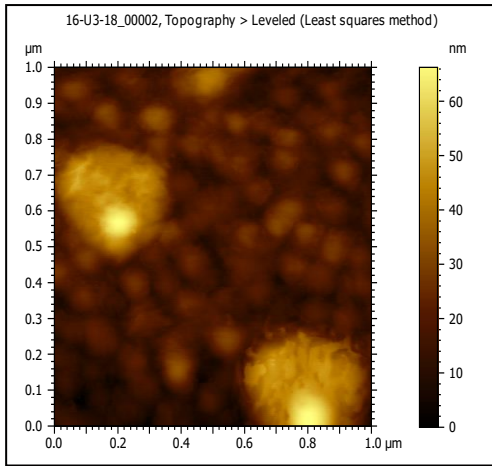
(f)



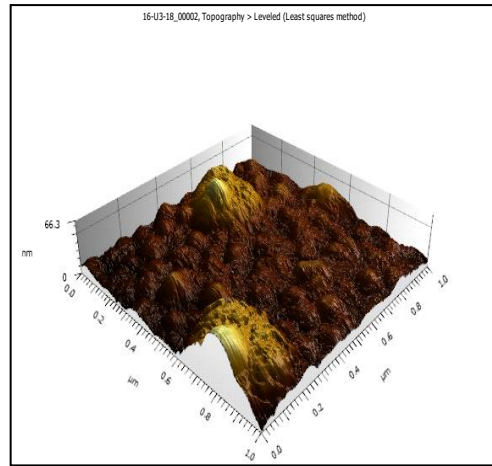
(g)



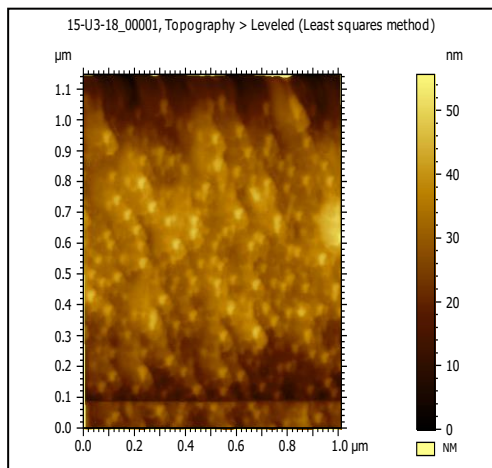
(h)



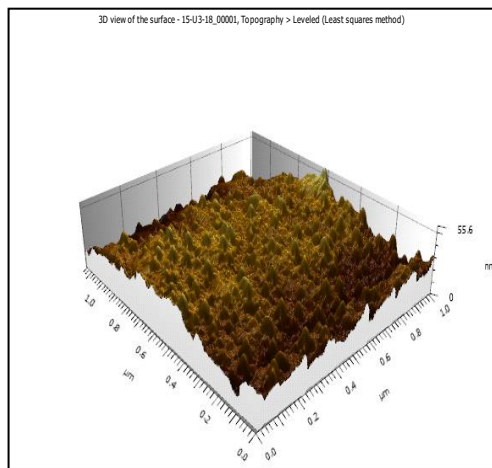
(i)



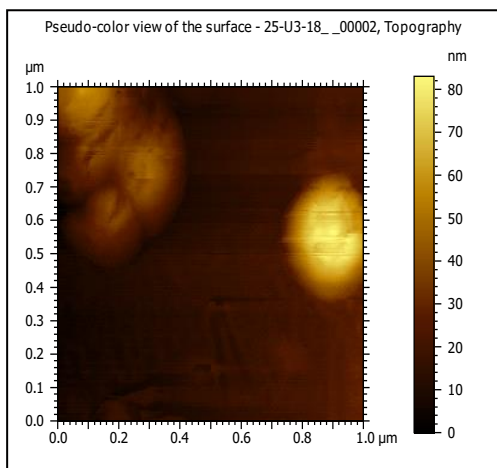
(j)



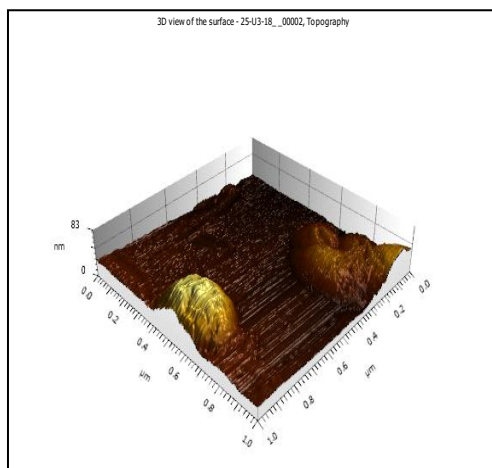
(k)



(l)



(m)



(n)

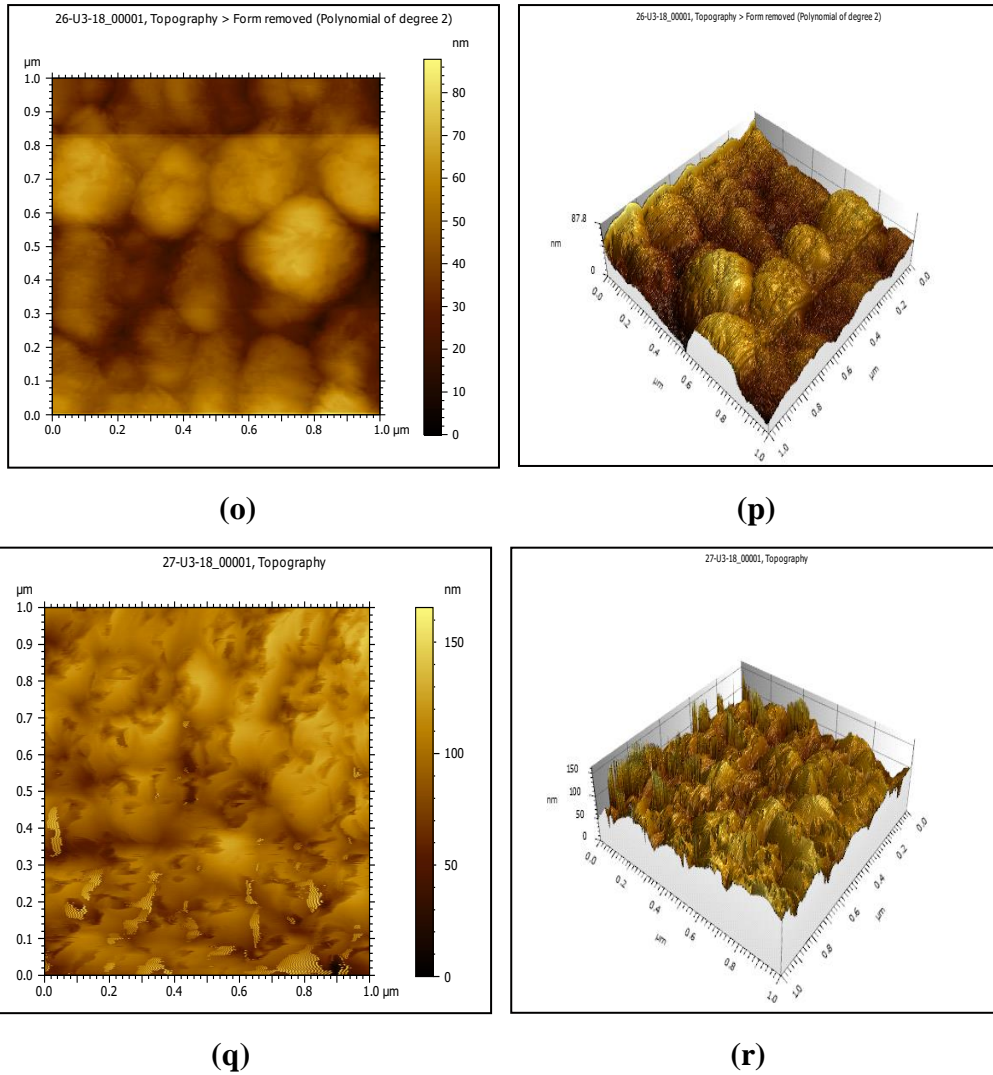


**Fig. 6.8: AFM analysis of i-ZnO thin film deposited at (a and b) 10 mTorr, (c and d) 5 mTorr, (e and f) 1 mTorr), 150 W and thickness 500 nm and AZO thin film at RT, (g and h) 300 nm, (i and j) 400 nm and (k and l) 500 nm) and ST-215 °C, (m and n) 300 nm, (o and p) 400 nm and (q and r) 500 nm.**

2D and 3D AFM images of i-ZnO and AZO thin films for topographical analysis were carried out using AFM Keysight 5500 Scanning Probe Microscope (Mode-AFM) instrument are shown in Fig. 6.8. The surface structure and texture of i-ZnO thin films deposited at 10 mTorr is shown in Fig. 6.8 (a and b) consist of a bunch of columnar rods at a certain inclination angle interspersed over the substrate surface. Growth is non-uniform over the surface and root mean square roughness ( $R_{rms}$ ) value of about 52.50 nm. On decreasing deposition pressure

to 5 mTorr as shown in Fig. 6.8 (c and d) has a similar growth structure to film deposited at 10 mTorr, but here bunches of columnar rods have well-defined grain boundaries, and these rods have uniform growth coverage over the substrate surface. Instead of c-axis orientation, columnar rods have inclined growth direction to the substrate surface and the roughness  $R_{rms}$  value is 72.28 nm. However, the formation of voids or surface defects such as vacancies, interstitials, and dislocations can easily occur due to the misalignment of atoms during the growth stage. Conformal coverage of i-ZnO thin film was observed at deposition pressure 1 mTorr shown in Fig. 8 (e and f). From the results, shown in Fig. 6.8 (e and f) it is depicted that growth is in the c-axis direction with no grain boundaries, and surface roughness decrease to 17.81 nm. For AZO thin films deposited at 10 mTorr with the thickness (300, 400, and 500 nm) and PRF 100 W, the structure and texture of films are dependent on thickness and substrate temperature i. e. RT and 215 °C. At RT, 300 nm AZO thin films have hillock topography. AZO hillocks interpose among themselves and have few numbers of valleys with roughness  $R_{rms}$  value 132.3 nm. Circular and uniform grain texture has formed with thickness 400 nm shown in Fig. 6.8 (i and j). Here surface roughness  $R_{rms}$  reduced drastically to 12.42 nm. The amalgamation of crystallites results in homogenous and grain boundary-free structures along with the c-axis direction. Sharp and tapered hillocks formed when thickness increase to 500 nm shown in Fig. 6.8 (k and l). Anisotropy in structure may be due to an increase in density of structure and reduced sticking coefficient due to which roughness  $R_{rms}$  increased to 152.5 nm. In presence of ST-215 °C, AZO film with a thickness of 300 nm shown in Fig. 6.8 (m and n) form gibbous structure having roughness  $R_{rms}$  value 114.8 nm interspersed all over the surface. Surprisingly, ST-215 °C, increase in thickness 400 nm Fig. 6.8 (o and p) overlapped gibbous structure formed with reducing surface roughness  $R_{rms}$  to 14.11 nm. Few but large grains formed over the substrate surface. More dense coalescence occurred when thickness increase to 500 nm shown in Fig. 6.8 (q and r). Between gibbous structures, vertical columns with uneven heights have been grown. Due to which surface roughness  $R_{rms}$  increase to 17.46 nm. The surface topography described above is dependent on deposition parameters (pressure, power, thickness, and substrate temperature. The results are well in agreement with the structure zone model proposed by John. A. Thornton [36].

The ratio of substrate temperature ( $T_s$ ) to Melting temperature ( $T_m$ ) describes the microstructural growth of the thin film. According to his proposed model, the topographical texture of i-ZnO and AZO films refers to zone 1 and zone T where  $T_s/T_m < 0.3$ . For i-ZnO and AZO thin films,  $T_s$  (297.15 K),  $T_s$  (488.15 K) and  $T_m$  (2253.15 K) ratio of  $T_s/T_m$  is 0.13 and 0.21. In 1969, Mouchan and Demichinhn (MD) [37] also proposed a thin film growth model in which they stated that tapered columns with voided boundaries structure are formed when  $T_s/T_m$  is 0.3. Growth of thin-film involves primarily surface diffusion process which is surface smoothing effects and secondly atomic shadowing effect along a preferential direction at an oblique angle. Due to the atomic shadowing effect, incoming energetic particles proceed towards the substrate surface at an oblique angle and are subjugated by higher surface points such as hills. The surface becomes rough columns and can cause sidewall growth at the surface during normal angle deposition. One another parameter that is important during growth is the sticking coefficient dependent on experimental growth parameters and substrate surface morphology. Incoming particles may stick or re-emit (re-sputter) from their impact point. Redeposition of energetic particles on the valley surface occurs when the re-sputtering of adatoms takes place by energetic atoms/ions. Height of surface locations due to the shadowing effect and presence of re-emitted particles that can travel long distances are responsible for growth structure. Re-emission leads to a smooth surface whereas the shadowing effect leads to a rough surface. Low-velocity incoming atoms possess a trajectory path and due to the presence of atom-atom attractive potentials, they are captive by an adjacent aggregate of atoms at the surface; this generates voids during the initial growth process. To fill voids, either substrate temperature should be raised so that enough surface diffusion of adatoms occurs or incoming particles must have enough energy so that voided boundaries can be filled by the momentum exchange process.

### 6.3.5 Scanning Electron Microscopy Analysis

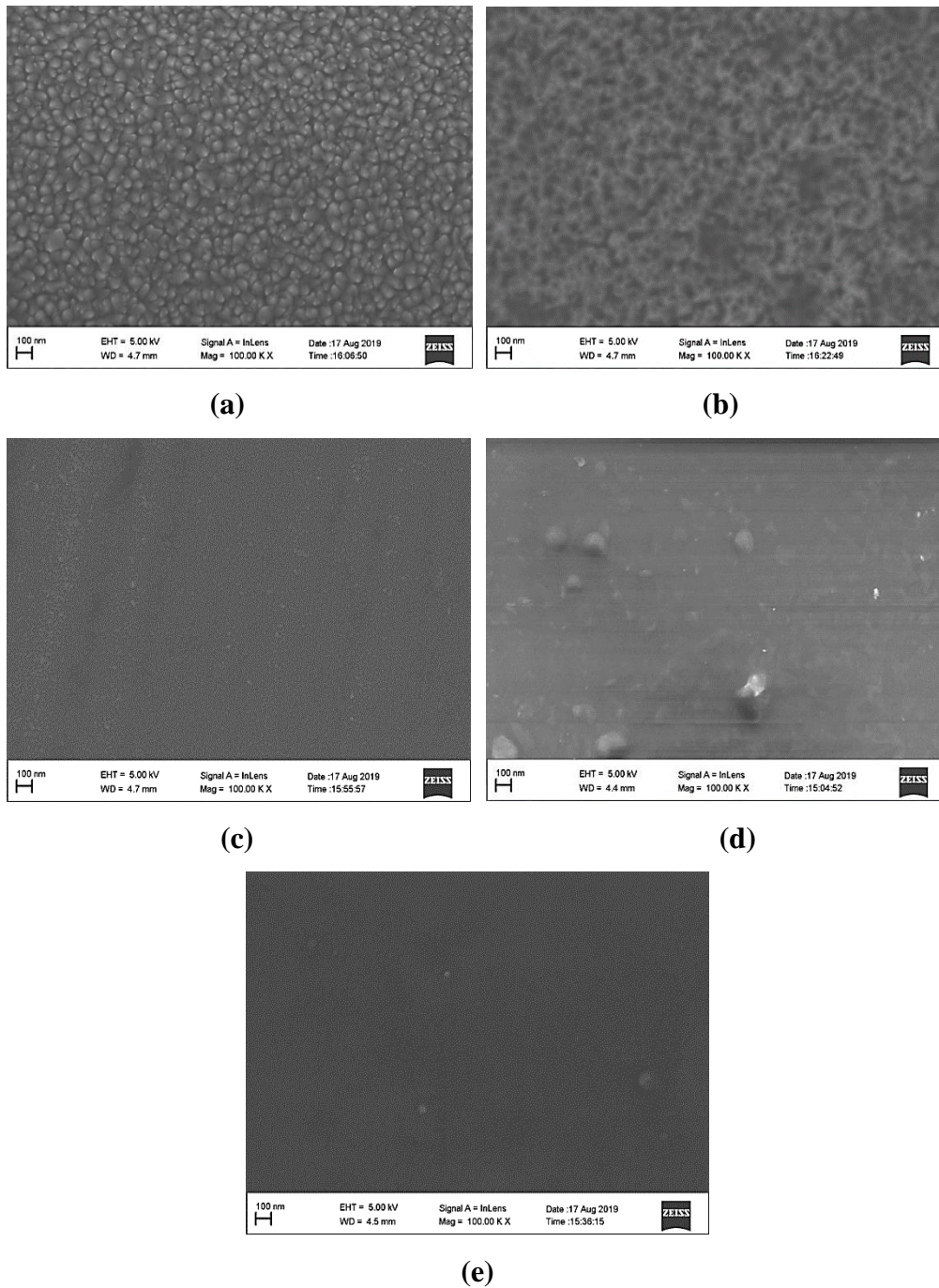


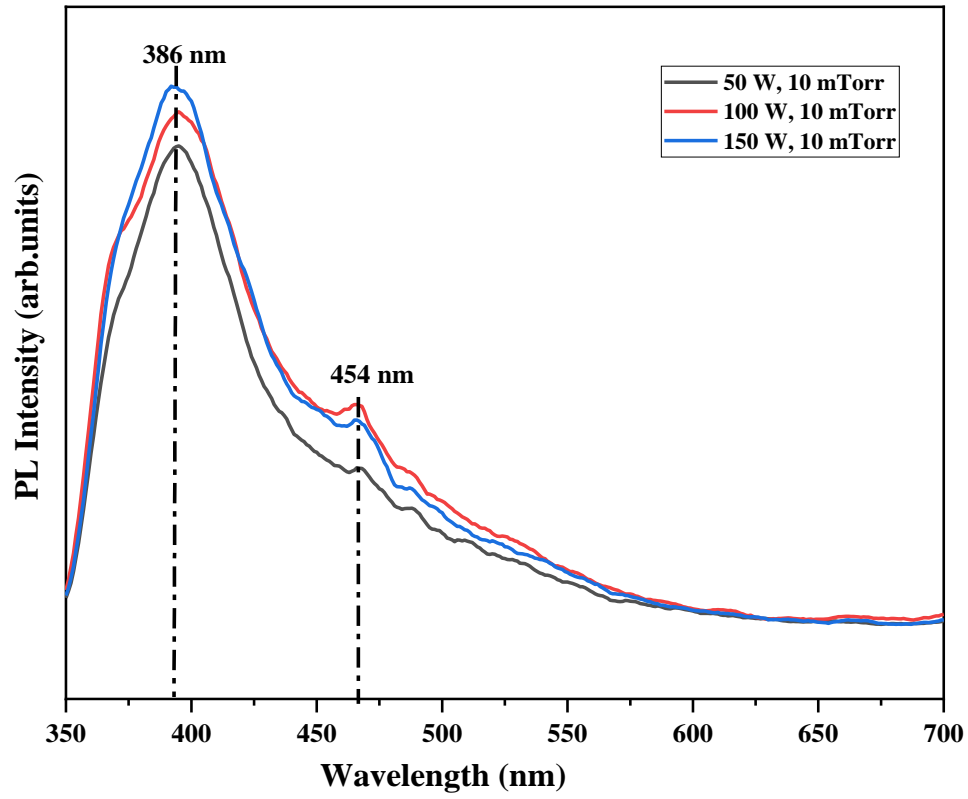
**Fig. 6.9: Scanning Microscopic image of AZO thin film (a) RT, (b) ST-215 °C and i-ZnO thin films (c) 10 mTorr, (d) 5 mTorr and (e) 1mTorr.**

Scanning Electron Microscopic top view images of AZO and i-ZnO thin films shown in Fig. 6.9 (a-e) provides a clear picture of the microstructural morphology of thin film formed due to variable deposition pressure and

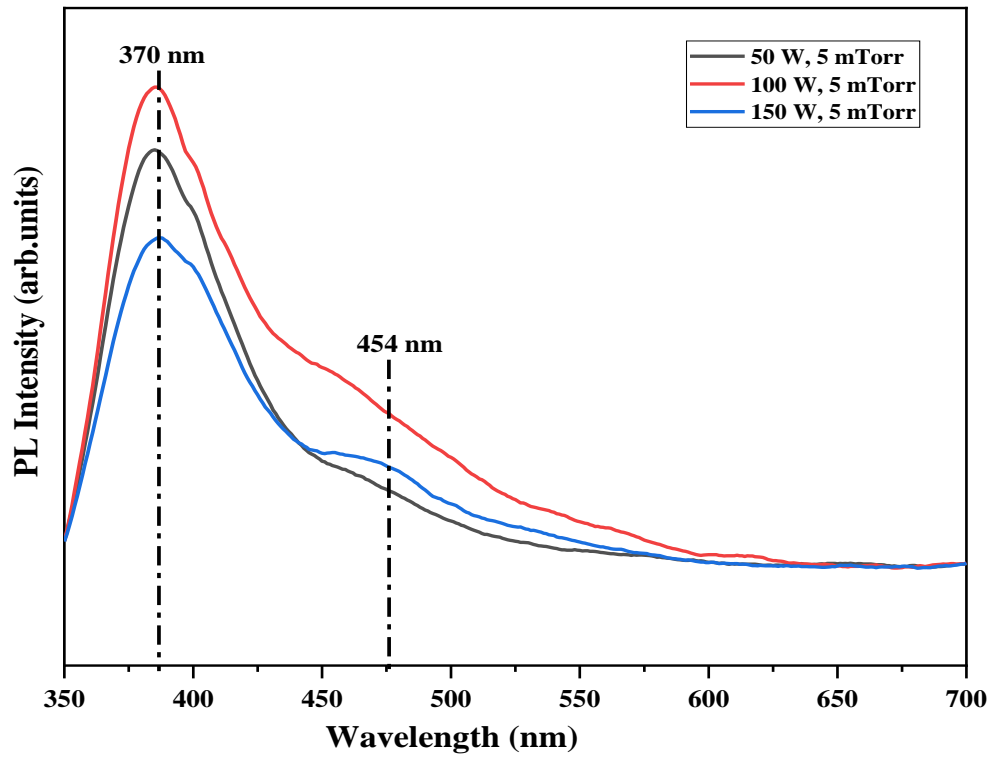
substrate temperature. AZO thin film deposited at RT at 10 mTorr with PRF 100 W as shown in Fig. 6.9 (a) have a uniform and well-defined geometric grain structure with perceptible voided grain boundaries. As the ratio of  $T_s/T_m$  is 0.13 and according to the zone structure model, these types of microstructure refers to zone 1. In the presence of ST-215 °C shown in Fig. 6.9 (b), thin-film has a similar microstructure to neural network structure [38]. These results also well agree with the zone structure model; here  $T_s/T_m$  value is 0.21 that represents Zone T. Of course, both zone 1 and zone T have columnar growth, but the topography is different. In the case of i-ZnO thin film deposited at 10 mTorr and PRF 150 W shown in Fig. 3.9 (c) possess undulating growth morphology while decreasing pressure to 5 mTorr shown in Fig. 3.9 (d), improper surface diffusion of incoming atoms takes place. Non-uniform aggregate forms on the surface, but further reducing the deposition pressure to 1 mTorr shown in Fig. 3.9 (e), aggregates reduce to a very large extent and the planar uniform surface was formed. It is assumed that at 1 mTorr, the incoming atoms have kinetic energy to get fully adsorbed on the substrate surface and avoiding void formation. i-ZnO deposited at 5 mTorr possess Stranski- Krastanov growth mode while at 1 mTorr layer by layer i. e., Frank Vander Merwe growth mode appeared.

### 6.3.6 Photoluminescence Analysis

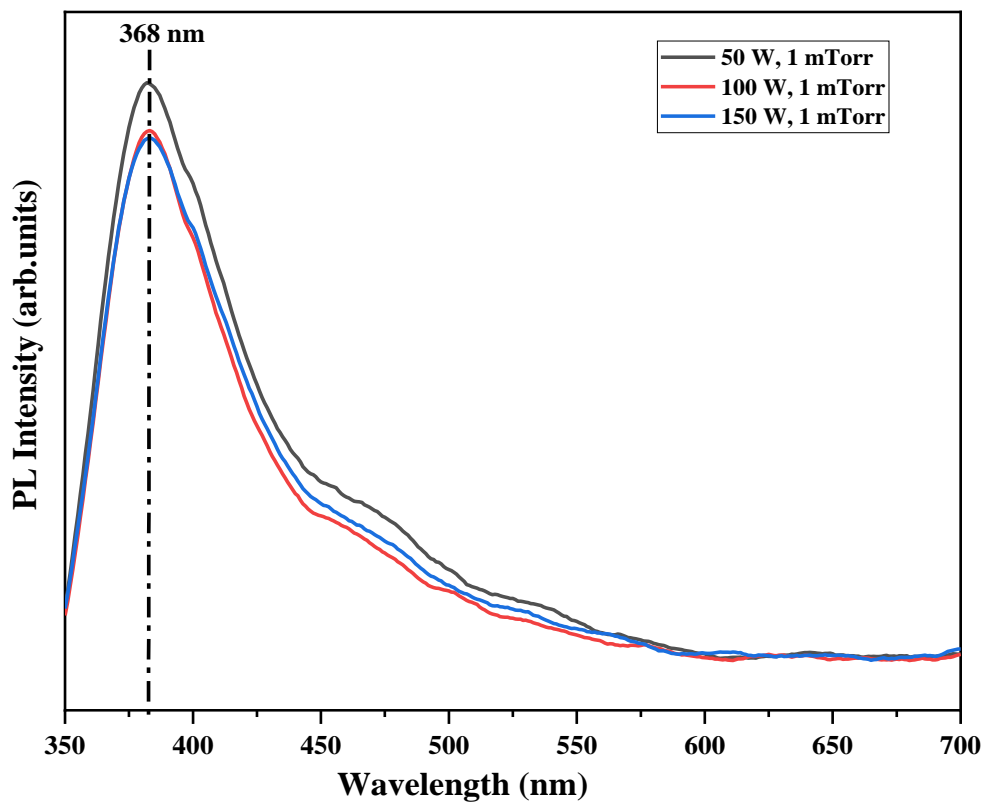
PL emission spectra of i-ZnO thin films are shown in Fig. 3.10 (a), (b), and (c). PL measurements were carried out at room temperature. The Xenon lamp was used as a source with an excitation wavelength of 245 nm. We have investigated the effect of deposition pressure on the PL properties of i-ZnO thin films. The experimental data are fitted by a multi-peak Gaussian shape to identify the contribution of various defects and impurities. The thickness of all i-ZnO thin films is kept at 50 nm. In Fig. 3.10 (a), the emission spectra are at 386 nm and another peak at 454 nm. The major peak at 386 nm corresponds to the near-UV region and 454 nm in the visible region. Near UV- band, the emission is due to the excitation recombination of ZnO taking place through an excitation-excitation



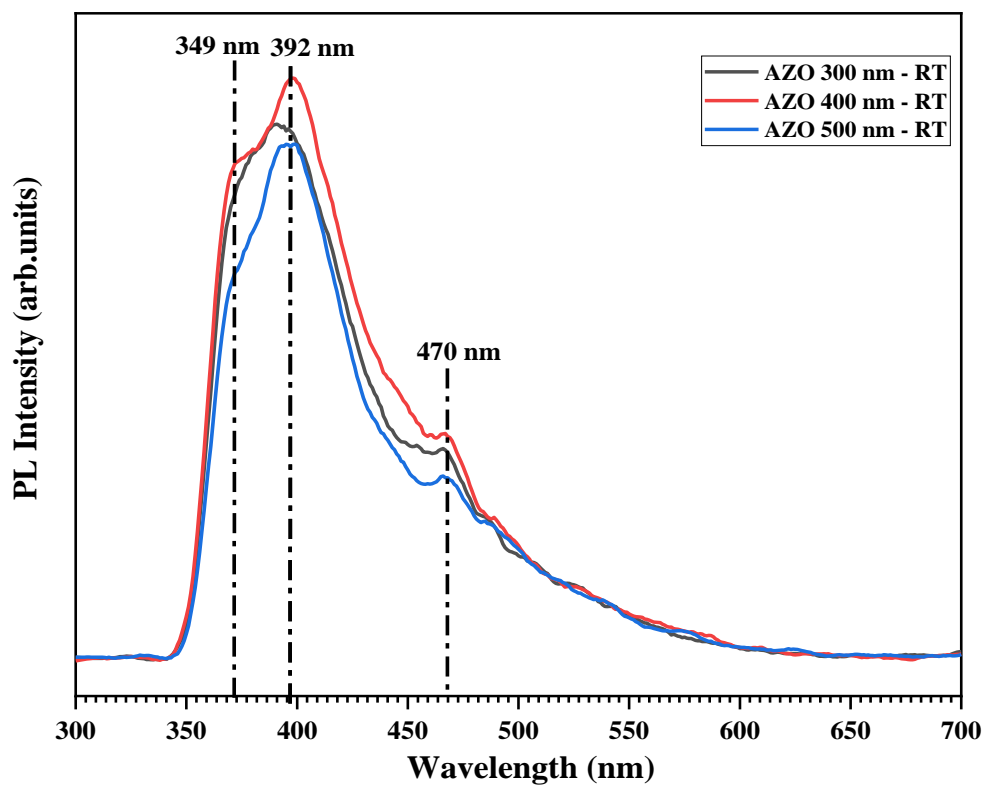
(a)



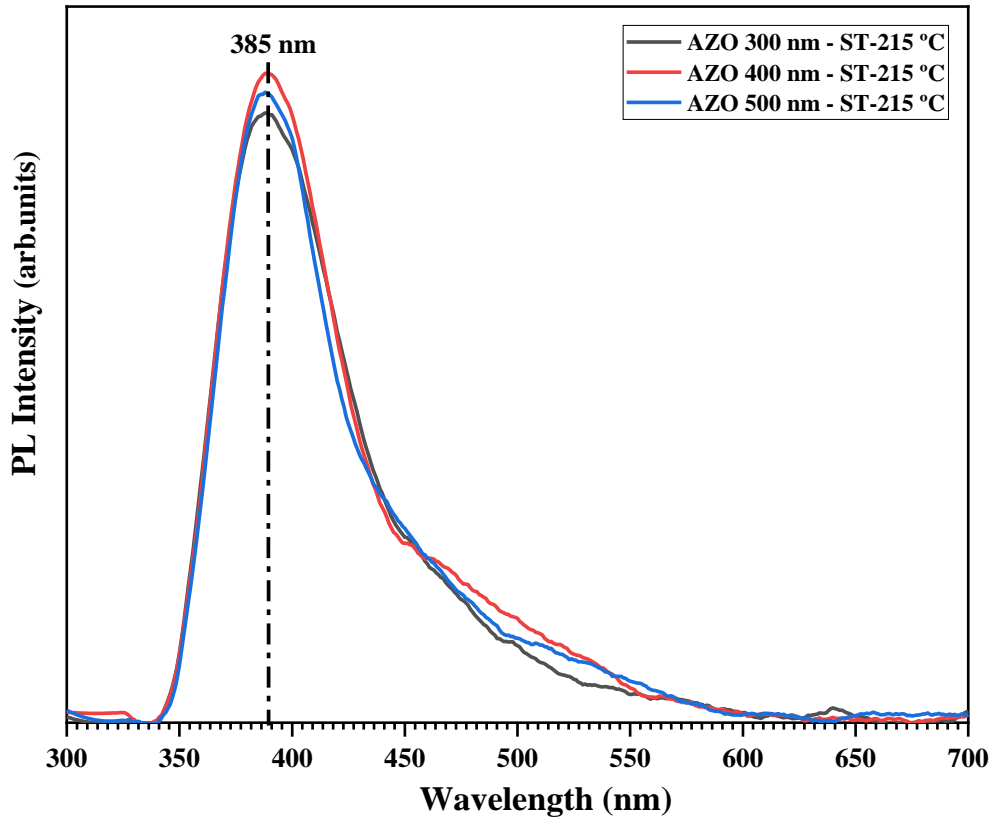
(b)



(c)



(d)



(e)

**Fig. 6.10: Photoluminescence (PL) emission spectra of i-ZnO thin films deposited ((a) 10 (b) 5 and (c) 1 mTorr), and AZO thin films ((d) RT and (e) ST-215 °C).**

collision process. As the deposition pressure decreases from 10 mTorr to 1 mTorr, the minor peak disappears which may be due to a decrease in defects or impurities. As high deposition power increases, the intensity of PL emission spectra decreases which confirms the reduction of defects. It is believed that zinc I interstitial/oxygen vacancies are donor impurities and oxygen interstitial/zinc vacancies are acceptors in the ZnO structure. The edge luminescence transition may correspond to the luminescence emission of a free exciton, excitons bound to neutral donors, and of their two-electron satellite (TES) [39, 40]. The cause of the major peak is near band edge emission of i-ZnO thin films whereas the minor peak may be due to electron transition from a shallow donor or electron transition from  $Z_{ni}$  to the  $V_{Zn}$ . Fig. 3.10 (d and e) represent PL spectra for AZO thin film deposited at pressure 10 mTorr, PRF

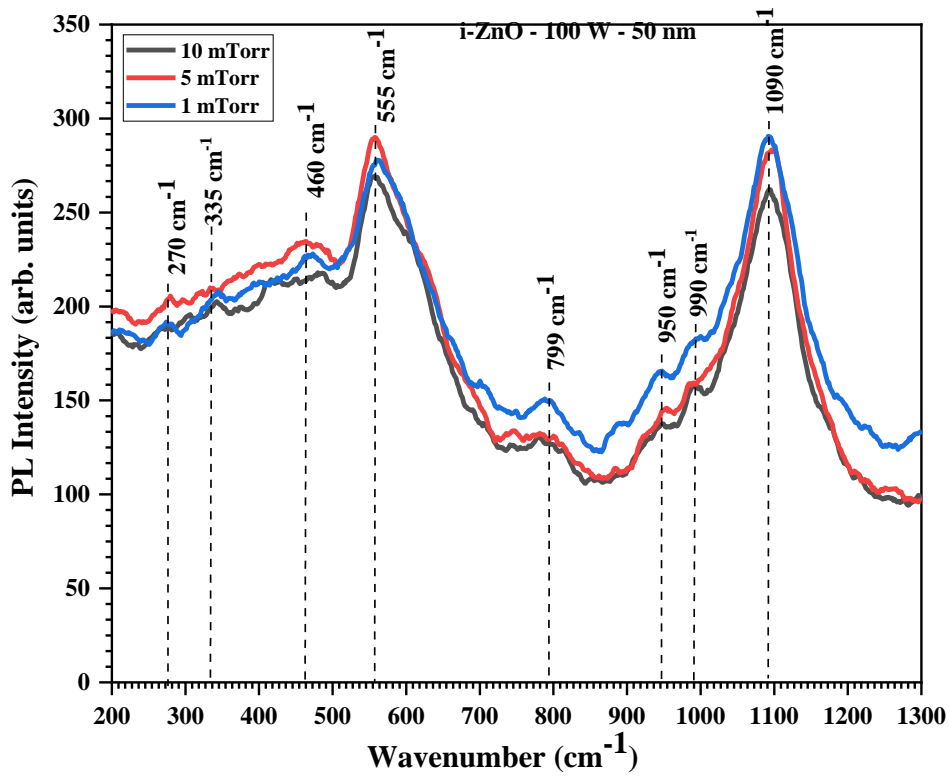
100 W, and thickness (300, 400, and 500 nm) at RT and ST-215 °C. At RT first peak at 349 nm was observed having 3.57 eV energy which is close to the Bandgap of AZO and another peak very close to it i. e. around 392 nm was observed having energy 3.17 e.V. This peak indicates transition followed by emission due to electron-electron collision near the band edge. Another peak at 470 nm depicts the presence of defects that give to green luminescence. But the method we adopted for deposition does not supply any oxygen atom. Therefore, this peak is near to the green luminescence band with very low intensity. There may be a probability of the formation of Zinc vacancy (V<sub>zn</sub>) due to its energy formation. V<sub>zn</sub> is a double acceptor having a transition level of  $\epsilon(0/-)$  and  $\epsilon(-2/2-)$ . Remarkably no such green luminescence was observed for AZO thin film deposited at ST-215 °C except near band edge at 385 nm [41-44].

### 6.3.7 Raman Spectroscopic Analysis

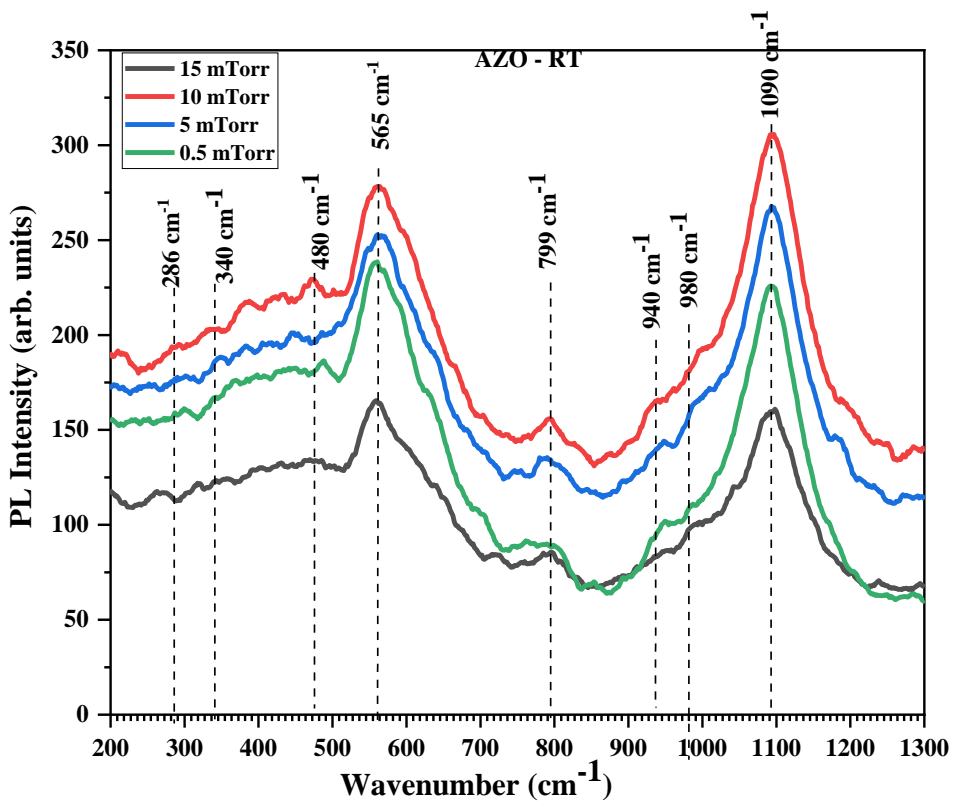
Fig. 6.11 represents Raman scattering of i-ZnO and AZO thin films recorded using instrument Model Horiba XploRa plus, (France) with excitation wavelength 532 nm in the range 200-1300  $\text{cm}^{-1}$ . 4C6v (P63mc) is a space group of ZnO with 12 phonons, 3 acoustic (LA+TA), and nine optical (LO, TO) modes. Irreducible representation of zone center optical phonon is given by the following equation (6.4):

$$T_{\text{opt}} = A_1 + E_1 + 2E_2 + 2B_1 \quad (6.4)$$

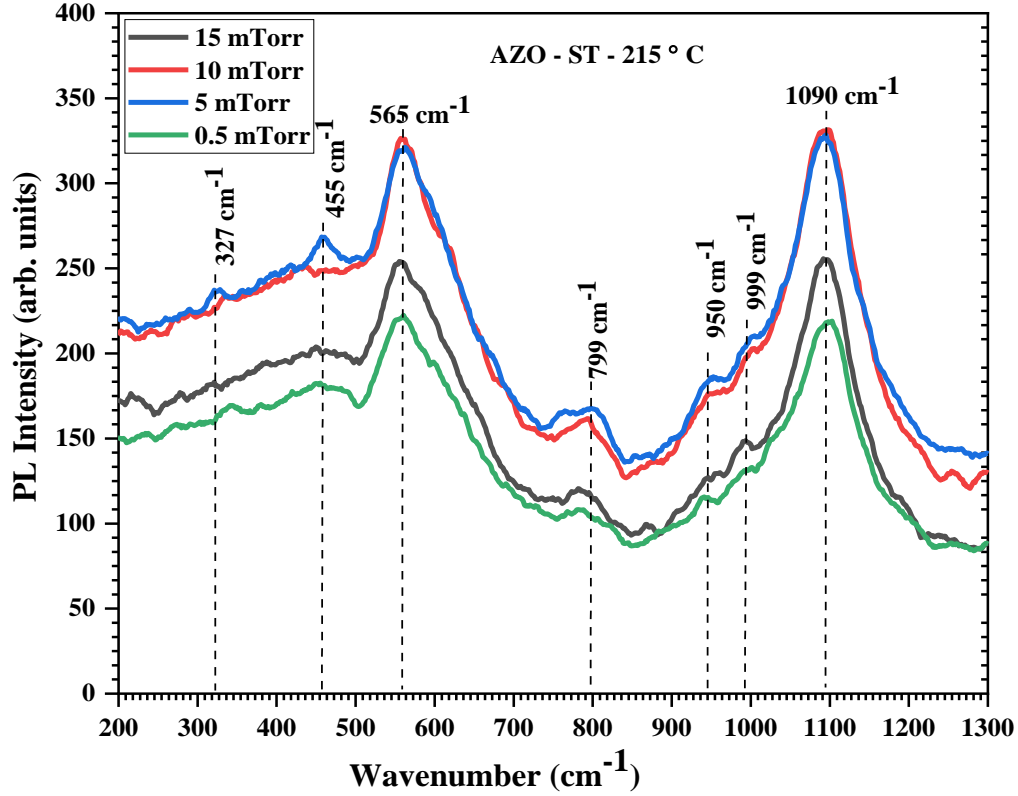
Both, Raman and IR active modes are A<sub>1</sub> and E<sub>1</sub> which are polar modes while E<sub>2</sub> mode is non-polar and Raman active only [45, 46]. In Fig. 6.11 (a), a peak at intermediate low-frequency regime i. e. 335  $\text{cm}^{-1}$  was observed for i-ZnO thin films but a slight shift towards higher frequency was observed as deposition increase to 10 mTorr. For AZO films deposited at RT shown in Fig. 6.11 (b), the peak shifted to 340  $\text{cm}^{-1}$  and was less intense and for AZO ST-215 °C shown in Fig. 6.11(c), the



(a)



(b)



(c)

**Fig. 6.11: Raman spectra emission spectra of i-ZnO thin films deposited (a) (10, 5 and 1 mTorr), AZO thin films at (b) RT and (c) ST-215 °C.**

peak wave number reduces to  $327\text{ cm}^{-1}$ . This peak must dominate A1 symmetry with low  $E_2$  high and  $E_1$  low components. Similarly, the difference in B1high and B1low components possess A1 symmetry at frequency  $270\text{ cm}^{-1}$  for i-ZnO while for AZO at RT frequency shifts to  $286\text{ cm}^{-1}$ [47]. Another A1 symmetry i.e., LA along with M-K points where phonon dispersion is flat, shift in peak broad was observed at  $460\text{ cm}^{-1}$  for i-ZnO films deposited at 1 mTorr, while for 5 mTorr slight intensity and broadness decrease but 10 mTorr pressure it shifted to  $480\text{ cm}^{-1}$ . A similar peak at  $480\text{ cm}^{-1}$  was only observed for AZO films deposited at 10 mTorr pressure RT while for ST-215 °C and other deposition conditions it was the only flat band. A highly intense peak at  $565\text{ cm}^{-1}$  was recorded. This peak refers to A1 (LO) vibration mode. A1 (LA+TA) mode  $790\text{ cm}^{-1}$  was observed with the Brillouin zone (M-K). A weak mode A1 (LO) was recorded for all i-ZnO thin films at  $555\text{ cm}^{-1}$  which is highly shifted towards the lower wavenumber compared to  $574\text{ cm}^{-1}$  [48]. This mode may be assigned to

the First-order system or second-order symmetry where frequency corresponds to both optical and acoustic phonon combination. Similar mode for AZO thin films deposited under RT and ST-215 °C but here frequency shift was observed at higher wavenumber. From this, one can infer that  $565\text{ cm}^{-1}$  tends towards First order symmetry mode. Well, all samples possess  $790\text{ cm}^{-1}$  and  $1090\text{ cm}^{-1}$  which originates from glass substrate [49]. A combination of four Brillouin zone points i. e. L-M-K-H with A1 (2TO) symmetry was present at  $980\text{ cm}^{-1}$  in all samples.

## Conclusions

In conclusion, the passivator and good charge collector layer for CIGS solar cell module on a 2 sq-inch glass substrate was studied. i-ZnO and AZO thin films were prepared using the RF sputter technique. The i-ZnO thin film was deposited using an in-house fabricated 2inch diameter sputter target. AZO thin film deposited at 10 mTorr, 100 W, RT with thickness 400 nm. This AZO thin film has good crystallographic orientation along the (002) plane and has a crystallite size of 25.18 nm. i-ZnO deposited at 151 W, 1 mTorr with thickness 50 nm possess low Urbach energy, i. e., 0.702 meV and meanwhile AZO thin film deposited at 100 W, 10 mTorr, RT with thickness have 0.4302 meV. This signifies low structural defects in both thin films and matches well in agreement with characterization reports. The estimated optical band gap energy for AZO was 3.35 eV, optical transmittance 85-90 % for a large number of photons. Around 0.05 eV Burstein-Moss shift was witnessed for above mentioned AZO thin film. Topographical and microstructural studies i-ZnO and AZO thin film reveal that depending on deposition parameters especially, on thickness, the structure, texture, and conformal coverage varies. Due to the presence of grain boundaries, the resistivity of AZO thin film is affected. The optimized AZO thin film has a resistivity in order of magnitude,  $10^{-4}$ , which serves as a good charge collector from the CIGS solar cell module. Photoluminescence and Raman spectra of i-ZnO and AZO thin films show material characteristics with defects and impurities as well as structure symmetry in Raman active mode.

## References

- [1] Arman Ghasedi, Ehsan Koushki, Mohammad Zirak, and Hassan Alehdaghi, *Appl. Phys. A*, **126** (2020) 474-1-474-9.
- [2] Deepak Punetha, Rashmi Ranjan, and Saurabh Kumar Pandey, *International Conference on Inventive Research in Material Science and Technology, AIP Conference Proceedings* 1966, edited by S. Sahulhameedu, et. al. (American Institute of Physics, Coimbatore, India, (2018) 020008-1- 020008-7.
- [3] K. Kandpal, and N. Gupta, *Microelectronics International*, **35** (2018) 52-63.
- [4] Xiaotong Zhang, Yu Qiu, Dechao Yang, Bing Li, Heqiu Zhang and Lizhong Hu, *RSC Adv*, **8** (2018)15290-15296.
- [5] Anisa Myzaferi, Asad J. Mughal, Daniel A. Cohen, Robert M. Farrell, Shuji Nakamura, James S. Speck, and Steven P. DenBaars, *Opt. Express*, **26** (2018) 12490-12498.
- [6] E. Q. B. Macabebe, C. J. Sheppard, and E.E. van Dyk, *Physica B*, **404** (22) (2009) 4466-4469.
- [7] Fredrik Larsson, Jan Keller, Marika Edoff, and Tobias Törndahl, *Thin Solid Films*, **633** (2017) 4466-4469.
- [8] Sung Hae Lee, Se Hoon Han, Hyun Suk Jung, Hyunjung Shin, Jagab Lee, Jun Hong Noh, Sangwook Lee, In Sun Cho, Jung Kun Lee, Jinyoung Kim, and Hyunho Shin, *J. Phys. Chem. C.*, **114** (2010) 7185-7189.
- [9] Khalid Mahmood, Bhabani Sankar Swain and Hyun Suk Jung, *Nanoscale*, **6** (2014) 9127.
- [10] F. Z. Bedia, A. Bedia, M. Aillerie, N. Maloufi, F. Genty, and B. Benyoucef, *Energy Procedia*, **50** (2014) 853-861.
- [11] Z. Ben Ayadi, H. Mahdhi, K. Djessas, J. L. Gauffier, L. El Mir, and S. Alaya, *Thin Solid Films*, **553** (2014) 123-126.
- [12] T. Prasada Rao and M. C. Santhoshkumar, *Appl Surf Sci*, **255** (2009) 4579-4584.
- [13] Hiroyuki Kato, Michihiro Sano, Kazuhiro Miyamoto and Takafumi Yao, *Jpn. J. Appl. Phys*, **42** (2003) L 1002-L 1005.

- [14] O. Pagni, G. R. James, and , A. W. R. Leitch, *phys. stat. sol. (c)*, **1(4)** (2004) 864-867.
- [15] M. Dutta, S. Mridha, and D. Basak, *Appl Surf Sci*, **254** (2008) 2743-2747.
- [16] Y. Yamamoto, K. Saito, K. Takahashi, and M. Konagai, *Sol. Energy Mater. Sol. Cells*, **65** (2001) 125-132.
- [17] Menon Rashmi, K. Sreenivas and Gupta Vinay, *J. Appl. Phys*, **103** (2008) 094903.
- [18] Chan Kim, Hyun Jun Jo, Dae Hwan Kim, Dae Ho Son, Dong Ha Lee and Ilsu Rhee, *Mol. Cryst. Liq. Cryst*, **565** (2012) 52-58.
- [19] Sanjay R. Dhage and Amol C. Badgujar, *J. Alloys Compd.*, **763** (2018) 504-511.
- [20] J. R. Ray, M. S. Desai, C. J. Panchal, and P. B. Patel, *J. Nano-Electron. Phys*, **3** (2011) 755-765.
- [21] Ping Tang, Bing Li, and Lianghuan Feng, *Ceramic Internationals*, **44** (2018) 4154-4157.
- [22] A. P. Roth, J. B. Webb, and D. F. Williams, *Solid State Commun*, **39** (1981)1269-1271.
- [23] B. E. Sernelius, K. Berggren, Z. Jin, I Hamberg I and C. G. Granqvist, *Phys. Rev. B*, **37** (1988) 10244-10247.
- [24] J. G. Lu and S. Fujita, *J. Appl. Phys*, **101** (2007) 083705-1-083705-7.
- [25] Anderson Janotti and Chris G. Van de Walle. *Phys. Rev. B*, **76** (2007) 165202-1-165202-22.
- [26] K. G. Saw, N. M. Aznan, F. K. Yam, S. S. Ng, and S. Y. Pung ,. *PLoS ONE*, **10 (10)** (2015)1-17.
- [27] H. Rotella, Y. Mazel, S. Brochen, A. Valla, A. Pautrat, C. Licitra, N. Rochat, C. Sabbione, G. Rodriguez and E. Nolot, *J. Phys. D: Appl. Phys*, **50** (2017) 485106 (1-7).
- [28] R. C. Rai, *J. Appl. Phys*, **113** (2013) 153508-1-153508-5.
- [29] S. Schönau, F. Ruske, S. Neubert, and B. Rech, *Appl. Phys. Lett*, **103** (2013) 192108.
- [30] Piet Van Mieghem, *Rev. Mod. Phys*, **64** (1992) 755-793.
- [31] J. I. Pankove, *Phys. Rev*, **140** (1965) A2059-A2065.

- [32] Anderson Janotti and Chris G. Van de Walle, *Appl. Phys. Lett*, **87** (2005) 122102-1-122102-3.
- [33] Tadatsugu Minami, Hidehito Nanto and Shinzo Takata, *J. Appl. Phys*, **24** (1985) L605-L607.
- [34] Naveen Kumar, Ashish Dubey, Behzad Bahrami, S. Venkatesan, Qiquan Qiao, and Mukesh Kumar, *Appl Surf Sci*, **436** (2018) 477-485.
- [35] Petr Novák, Jan Očenášek, Tomáš Kozák, and Jarmila Savková, *Thin solid films* **660** (2018) 471-476.
- [36] John A. Thornton, *In: Proceedings 31st Annual Technical Symposium on Optical and Optoelectronic Applied Sciences and Engineering*, 1987 San Diego, CA, United States., SPIE Vol. **821** Modeling of Optical Thin Films (1987) 95-103.
- [37] Tansel Karabacak, *J. of Nanophotonics*, **5** (2011) 052501-1-052501-18.
- [38] Dengyuan Song, Armin G. Aberle, and James Xia, *Appl Surf Sci*, **195** (2002) 291-296.
- [39] Rodnyi P. A. and Khodyuk I. V., *Opt Spectrosc*, **111** (2011) 776-785.
- [40] D. H. Zhang, Z. Y. Xue and Q. P. Wang, *J. Phys. D: Appl. Phys*, **35** (2002) 2837-2840.
- [41] Sukanta Bose, Rayerfrancis Arokiyadoss, P. Balaji Bhargav, Gufran Ahmad, Sourav Mandal, A. K. Barua, and Sumita Mukhopadhyay, *Mat Sci Semicon Proc.*, **79** (2018) 135-143.
- [42] A. I. Ali, C. H. Kim, J. H. Cho and Bog G. Kim, *J. Korean Phys. Soc*, **49** (2006) S652 - S656.
- [43] B. S. Li, Y. C. Liu, Z. Z. Zhi, D. Z. Shen, Y. M. Lu, J. Y. Zhang, X. G. Kong, and X. W. Fan, *Thin Solid Films*, **414** (2002)170-174.
- [44] S. B. Zhang, S. -H. Wei, and Alex Zunger, *Phys. Rev. B*, **63** (2001) 075205-1-075205-7.
- [45] Ramon Cuscó, Esther Alarcón-Lladó, Jordi Ibáñez, and Luis Artús, Juan Jiménez, Buguo Wang, and Michael J. Callahan, *Phys. Rev. B*, **75** (2007) 165202-1-165202-11.

- [46] C. A. Arguello, D. L. Rousseau, And S. P. S. Porto, *Phys. Rev*, **181**(1969) 1351-1363.
- [47] D. Canteli, S. Fernandez, C. Molpeceres, I. Torres, and J. J. Gandía, *Appl Surf Sci*, **258** (2012) 9447-9451.
- [48] C. Charpentier, P. Prod'homme, and P. Roca i Cabarrocas, *Thin Solid Films*, **531** (2013) 424-429.
- [49] Fred Joe Nambala, Jacqueline M. Nel, Augusto G. J. Machatine, Bonex W. Mwakikunga, Eric G. Njoroge, Kelebogile Maabong, Arran G. M. Das and Mmantsae Diale, *Physica B*, **480** (2016) 72-79.